RESEARCH ARTICLE

Mesoscale atmospheric processes over an Arctic fjord as observed during a research aircraft campaign in winter

Irene Suomi,[1] Timo Vihma,[1] Tiina Nygård,[1] Jörg Hartmann[2] & Christof Lüpkes[2]
[1]Finnish Meteorological Institute, Helsinki, Finland; [2]Alfred Wegener Institute for Polar and Marine Research, Bremerhaven, Germany

Abstract

Unique research aircraft observations were conducted within an Arctic fjord in Svalbard during three days in March 2013. Wijdefjorden is 110 km long, 5–15 km wide and has a north–south axis. Two-thirds of the fjord were covered by land-fast sea ice, but the northern part of the fjord was open. On two days the flow over the fjord was largely controlled by orographic channelling of the north-easterly wind, and on all three days a cold-air mass accumulated over the sea ice in the fjord and gradually propagated towards the open sea in the north. An ice breeze (analogous to land breeze) circulation, due to a strong temperature gradient across the sea-ice edge, was a key driver of the southerly near-surface wind over the fjord. On two days, the cold-air mass reached the open sea and the near-surface air mass warmed rapidly by several Kelvins. On one day, the channelled northerly flow pushed the cold-air mass to the south, from where it gradually propagated back to the north after the channelled flow had weakened. The results suggest that the channelling of the large-scale flow in the fjord can suppress the ice breeze to a shallow near-surface layer and even push the cold-air mass far south of ice edge. The near-surface air temperature and wind fields that were based on the Copernicus Climate Change Service Arctic Regional Reanalysis (CARRA) data set included large errors because CARRA did not have any sea ice in the fjord.

To access the supplementary material, please visit the article landing page

Keywords

Atmospheric boundary layer; orographic flow channelling; cold-air pool; ice breeze circulation; low-level jet; katabatic wind

Correspondence

Irene Suomi, Finnish Meteorological Institute, P.O. Box 503, FI-00101 Helsinki, Finland.
E-mail: irene.e.suomi@gmail.com

Abbreviations

ABL: atmospheric boundary layer
a.g.l.: above ground level
CARRA: Copernicus Climate Change Service (C3S) Arctic Regional Reanalysis
ERA5: European Centre for Medium-Range Weather Forecasts reanalysis data set, generation 5
ESA CCI: European Space Agency Climate Change Initiative
LLJ: low-level jet
OSI-450: European Organisation for the Exploitation of Meteorological Satellites Ocean and Sea Ice Satellite Application Facility SIC product
OSTIA: Operational Sea Surface Temperature and Sea Ice Analysis
SIC: sea-ice concentration
SICCI: European Space Agency Climate Change Initiative SIC product
SST: sea-surface temperature
TKE: turbulent kinetic energy

Introduction

Human activities in the Arctic are concentrated in coastal regions at locations typically surrounded by complex orography. Under the predominant stably stratified conditions in the ABL the orography has typically a strong impact on the near-surface wind and temperature conditions as well as on the dispersion of atmospheric pollutants. However, because of the harsh environment and the remoteness of the Arctic, extensive experimental data sets on the flow dynamics in the ABL over complex terrain are rare.

Since the pioneering theoretical analyses of Queney (1948) and Scorer (1949), orographic effects on mesoscale and local meteorological processes have been considered in numerous studies, some of them addressing the Arctic (Jonassen et al. 2020; Shestakova et al. 2020; Shestakova et al. 2022). Although reasonably well understood on the basis of dynamical theory (Heinemann & Klein 2002), observations and model experiments of individual orographic effects and katabatic winds are complicated by interactions of several simultaneous processes and boundary conditions in regions of complex orography (Vihma et al. 2014; Jonassen et al. 2020).

In mountain valleys with a straight axis, winds are typically from two main directions: up-valley or down-valley (e.g., Whiteman & Doran 1993; Nawri & Stewart 2008). According to Whiteman & Doran (1993) the main driving mechanisms for the winds along the valley are: (1) thermal, causing down-valley winds in the night time and up-valley winds in daytime; and (2) mechanical, which can be partitioned into (i) forced

Citation: *Polar Research* 2025, *44*, 9263, http://dx.doi.org/10.33265/polar.v44.9263

channelling, when the geostrophic wind has a component along the fjord axis either in the up- or down-valley direction, or (ii) pressure-driven channelling, when the geostrophic wind is perpendicular to the valley wind, and the valley wind is driven by the pressure difference along the valley. In the latter case, the wind within the valley is directed to the left (in the Northern Hemisphere) from the direction of the (quasi-)geostrophic wind at the height of the mountain tops. Typical for both forced channelling and pressure-driven channelling is that the transition between down-valley and up-valley flow takes place over a very small range of geostrophic wind directions perpendicular to the valley axis (Whiteman & Doran 1993).

Over Arctic fjords, the orography resembles conditions in mountain valleys, but the dynamical processes are often complicated by various factors: (1) in mountain conditions the valley bottom is typically gently sloping but the sea surface in fjords is flat; (2) the surface boundary conditions in a fjord typically change in time because of the mobile sea surface (ocean waves, currents) as well as sea-ice formation, drift and melt; (3) in most mountain valleys studied (Flamant et al. 2002; Mayr et al. 2007; Schnitzhofer et al. 2009) solar radiation plays a larger role than in Arctic fjords; and (4) mountain valleys lack the step changes in surface temperature, generated by the ice edge in fjords. In fjords in winter, the ice/snow surface temperature can be down to −30 °C and in extreme cases even lower, while the surface of the open sea remains close to the freezing point of about −1.8 °C. In both mountain valleys and fjords, katabatic or other downslope winds are often generated on the slopes, transporting cold air downwards.

The large thermal differences and the complex topography around fjords often generate non-local effects on the turbulent surface fluxes of momentum, heat and moisture. In a study of the ABL over the ice-covered Wahlenbergfjorden, in Svalbard, Mäkiranta et al. (2011) detected drainage flows transporting cold air over the sea ice, where the winds calmed down and a cold-air pool was generated. Over the sea ice, there was, however, more turbulence than the local surface-based wind shear could have generated, probably due to top-down mixing caused by the large wind shear above the cold-air pool (Mäkiranta et al. 2011).

On the basis of their analysis of tethersonde sounding data over Isfjorden and Kongsfjorden in Svalbard, Vihma et al. (2011) found that low-level temperature inversion properties were more strongly controlled by synoptic scale weather conditions above the mountain tops than by lower boundary conditions at the Earth's surface. However, LLJs, which they detected, were related to surface-driven katabatic winds. In Kongsfjorden, which was mostly covered by sea ice, the LLJs occurred above a cold-air pool that prevailed over the fjord ice. High-resolution model experiments by Kilpeläinen et al. (2011) revealed strong spatial variability of near-surface wind, temperature and humidity, as well as of the turbulent surface fluxes of sensible and latent heat in Isfjorden, Kongsfjorden and Storfjorden. For these variables, the magnitude of spatial variability within a single fjord was often comparable to the magnitude of temporal variability on synoptic timescales. Model sensitivity experiments without any topography revealed that the topography increased the spatial variability.

Research aircraft observations have been applied to study the ABL as well as the air–sea and air–ice interaction in the Arctic (e.g., Renfrew et al. 2008; Renfrew et al. 2009; Kristjánsson et al. 2011; Tetzlaff et al. 2014; Lüpkes & Gryanik 2015; Tetzlaff et al. 2015; Suomi et al. 2016; Heinemann 2018; Wendisch et al. 2019; Michaelis et al. 2020; Michaelis et al. 2021). However, flights over fjords have been rare, and the observed flow conditions have been such that the impacts of orography have been minimal, for example, over the wide Storfjorden (Vihma et al. 2003), or the flights have only passed the fjord mouth, yielding data on the outflow from fjords (Kristjánsson et al. 2011).

In March 2013, three research flights were carried out over the long, narrow Wijdefjorden in Svalbard. We analyse these observations here to investigate mesoscale dynamics and interactions of the ABL with the open sea and sea ice. Such observations can be considered as unique and are unlikely to be repeated since more restrictive limitations have been implemented in this area for environmental protection reasons. Our objective is to better understand fjordic mesoscale and boundary layer processes, such as channelling, barrier winds, downslope winds, flow across an ice edge (where the surface temperature gradient is strong), and fronts between warm and cold airmasses, and to distinguish primary challenges for the representation of the flow in fjords and related processes in high-resolution atmospheric reanalysis. To achieve the latter objective, we use data from CARRA (Yang et al. 2020). CARRA is a high-resolution (2.5 km) reanalysis data set that complements the ERA5 global reanalyses in 31 km resolution. Because of the high resolution of CARRA, it is expected to give more realistic results over the steep Arctic landscapes. The fjord that is the subject of this study is the second largest fjord in Svalbard. Yet its width is just 5–10 km, which is too narrow to be represented by the ERA5 reanalysis.

We begin with the description of the measurements and data, including research aircraft observations and the CARRA reanalysis data set, and explain the data

Citation: *Polar Research* 2025, *44*, 9263, http://dx.doi.org/10.33265/polar.v44.9263

processing methods. We then present the results that are based on the most extensive flight mission on 19 March, followed by a comparison to the conditions during two other days, 17 and 25 March, when there was only one saw-tooth pattern flight along the fjord available per day. This is followed by an evaluation of the CARRA reanalysis. After comparing our results with previous studies, we consider future perspectives.

Measurements, data and methods

Aircraft measurements

Research aircraft measurements were collected as a part of the Spring-Time Atmospheric Boundary Layer Experiment (e.g., Tetzlaff et al. 2015) over the long (110 km) and narrow (5–15 km) Wijdefjorden, in the northern parts of Svalbard (Fig. 1) on three days: 17, 19 and 25 March 2013. In the archipelago, the fjord is second only to Storfjorden in length. On a large scale it has a simple V-shaped structure horizontally, with an almost straight south-to-north axis, but the fjord is bounded by complex topography varying horizontally on scales of a hundred metres to kilometres (Fig. 1). The mountains on both sides of the fjord exceed 1000 m, the peaks on the eastern side reaching somewhat higher than on the western side. Maximum terrain elevations (Fig. 1c) on each side of the fjord were determined as the maximum height of the topography in a range ±1.5° of longitude zonally from the path of the saw-tooth pattern flight (all flight days) and the flight over the glacier near noon (on 19 March). The topography was obtained from Amante & Eakins (2009).

Instrumentation and data processing

The measurements used in this study, taken onboard the Polar 5 research aircraft, included air temperature, pressure and the three orthogonal wind components at

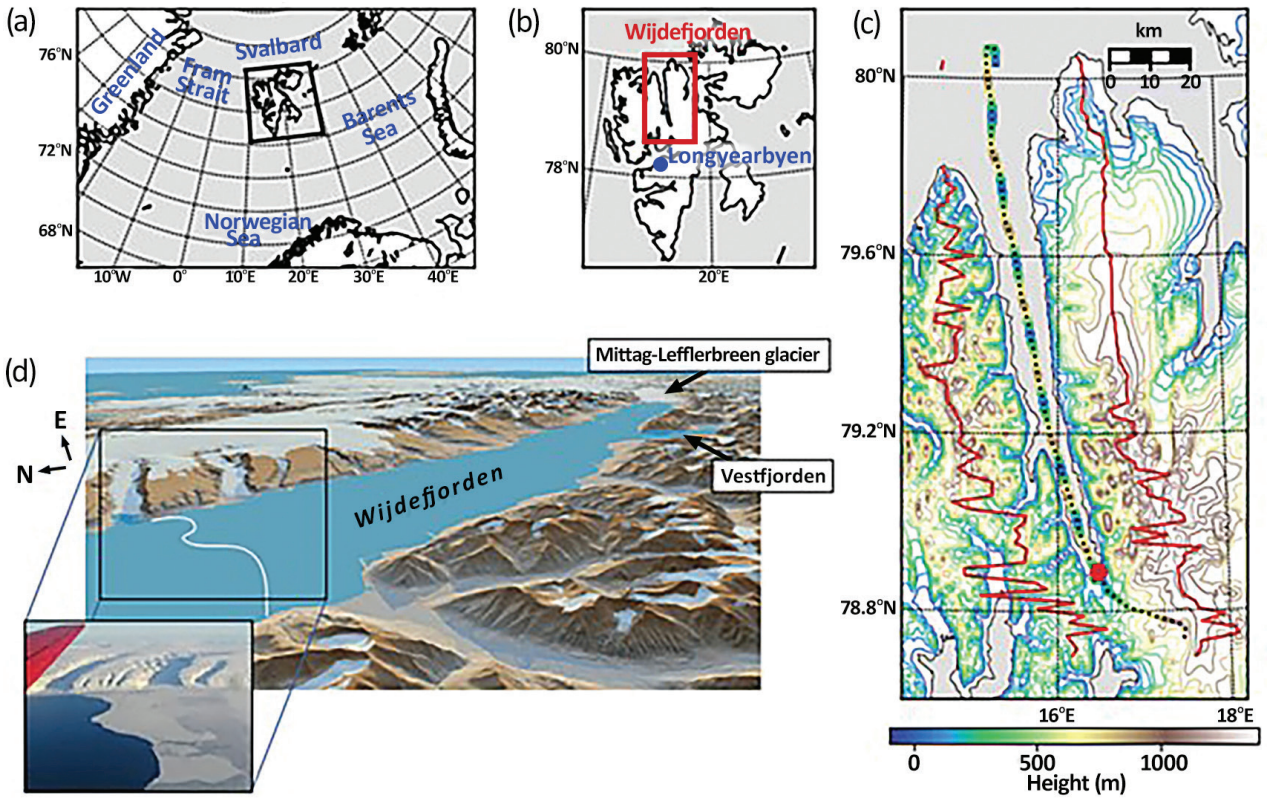

Fig. 1 The study region, Wijdefjorden, is located in (a) the European Arctic, in (b) the northern part of Svalbard. The colours in (c) show the topography around Wijdefjorden (Amante & Eakins 2009) and the height (m a.s.l.) of the flights down the glacier and along the saw-tooth pattern on 19 March 2013 (dotted lines). The location of the maximum terrain elevation in a range ±1.5° of longitude zonally from the flight path is shown as red lines, and the red dot shows the location of the reference point at the fjord head. (d) A graphic illustration of the mountains around Wijdefjorden (Norwegian Polar Institute, retrieved from https://toposvalbard.npolar.no on 2 February 2022). During the flights, the mountains were covered by snow and the fjord was ice-covered from the fjord head northward to about 72.5 km north of the fjord head, as shown in the photograph taken during the flight on 17 March 2013.

100 Hz frequency (Table 1). During the horizontal flights, the observed aircraft ground speeds varied between about 50 and 70 m s^{-1}, resulting in a spatial resolution of about 0.5–0.7 m. The wind components were measured using a five-hole probe and the temperature with a PT-100. These sensors were mounted on a 3-m-long nose boom. The height and the position of the aircraft were derived from GPS and Inertial Navigation System data. The Earth surface temperatures were measured with a KT-19 radiation thermometer with 10 Hz resolution. It measures in the wavelength range of 9.6 – 11.5 µm, and the measurement uncertainty is about 1 K (Tetzlaff et al. 2015). Flights consisted of horizontal and vertical profiles and saw-tooth patterns (Table 2). Profiles are considered as vertical when the flight altitude increases or decreases systematically during the flight. A saw-tooth pattern consists of multiple consecutive ascents and descents, that is, vertical profiles, along the fjord. The median flight path aspect ratio (change in flight altitude / horizontal distance) of the profiles is given in Table 2. The ratio varies from −83 to −39 m/km for descents and from +34 to +119 m/km for ascents. During horizontal flights the flight altitude also varied, up to 49 m from the mean (due to necessary flight manoeuvres). It is considered in turbulent flux calculations (see below), but in the calculation of other statistics along the horizontal flight paths we do not apply any flight altitude corrections.

The aircraft measurements presented here illustrate both the potential of small-scale airborne measurement techniques as well as their limits in the vicinity of topographic features and due to simultaneous changes in time and location. We therefore try to provide information on both the time and the location (height/distance/coordinates) of the measurements whenever possible. All research aircraft data were first divided into bins 500 m in length (vertical profiles, profiles along the glacier and the profiles along the saw-tooth patterns) or 2500 m in length (horizontal flights) along the flight path. We used a shorter bin width for the vertical profiles to reduce the effect of flight altitude changes in the statistics. With the aspect ratios given in Table 2, the layer thickness corresponding to a horizontal flight distance of 500 m amounts

Table 1 Observed parameters used in this study, instrumentation and accuracy of measurements on board the Polar 5 research aircraft.

Parameter	Description	Instrument	Measurement frequency	Accuracy (±)	Additional remarks
t_nm	time, ms since midnight		100 Hz		
lon	longitude	GPS	1 Hz	5 m	
lat	latitude	GPS	1 Hz	5 m	
h_a	height	GPS, INS	1 Hz	10 m	relative accuracies can be better
h_rad	height	radar altimeter		1 m	accuracy over water
ps	static pressure	Rosemount pressure transducer	100 Hz	0.1 hPa	
T	air temperature	PT-100	100 Hz	0.1 K	instrument mounted on the 3-m-long nose boom
u, v	wind velocity components (positive towards east and north, respectively)	Rosemount 858 five-hole probe	100 Hz	0.25 m/s	instrument mounted on the 3-m-long nose boom
w	wind velocity component (positive upwards)	Rosemount 858 five-hole probe	100 Hz	a few cm/s	accuracy given as a deviation from the mean; instrument mounted on the 3-m-long nose boom
u_a, v_a, w_a	aircraft velocity components (positive towards east, north and upwards, respectively)	GPS, INS	1 Hz	0.03 m/s	
RH	relative humidity	Vaisala HMT-333 (HUMICAP and temperature)	1 Hz	0.4 %	
KT19	Earth surface temperature	KT-19	10 Hz	1 K	Heimann radiation temperature measurement, based on IR measurements on the range 9.6–11.5 µm

Citation: *Polar Research* 2025, *44*, 9263, http://dx.doi.org/10.33265/polar.v44.9263

Table 2 Time, flight altitudes of profiles and horizontal flights and median flight aspect ratios of flight sections below 1 km a.s.l.

Date	Time (UTC)	Flight altitude (m a.s.l.)[a]	Flight aspect ratio (m/km)[b]	Flight pattern
17.3.2013	15:13 – 16:02	32 – 915	−77 / +98	Saw-tooth pattern along the fjord
19.3.2013	10:42 – 10:52	27 – 1716	−39	Profile down the glacier Mittag-Lefflerbreen
19.3.2013	10:52 – 11:01	28 – 2878	+115	Vertical profile up from the fjord head
19.3.2013	11:02 – 11:12	30 – 2879	−41	Vertical profile down to the fjord head
19.3.2013	11:12 – 12:03	39 (−7/+8)	-	Horizontal flight along the fjord
19.3.2013	12:06 – 12:14	54 – 2898	+96	Vertical profile at the mouth of the fjord
19.3.2013	12:15 – 12:21	1175 – 2891	−68	Vertical profile at the mouth of the fjord
19.3.2013	12:20 – 12:55	1159 (−21/+28)	-	Horizontal flight along the fjord
19.3.2013	13:02 – 13:40	1156 (−17/+20)	-	Horizontal flight on the western side of the fjord
19.3.2013	13:44 – 13:49	329 – 1156	−58	Vertical profile at the mouth of the fjord
19.3.2013	13:50 – 14:24	319 (±20)	-	Horizontal flight along the fjord
19.3.2013	14:25 – 15:10	28 – 913	−83 / +119	Saw-tooth pattern along the fjord
19.3.2013	15:10 – 15:47	36 (−7/+8)	-	Horizontal flight along the fjord
19.3.2013	15:48 – 15:51	52 – 1145	+85	Vertical profile up from the fjord head
19.3.2013	15:52 – 15:58	1158 (−10/+8)	-	Horizontal flight on the eastern side of the fjord
19.3.2013	15:59 – 16:06	1327 (−18/+13)	-	Horizontal flight on the eastern side of the fjord
19.3.2013	16:07 – 16:12	1318 (−13/+11)	-	Horizontal flight on the eastern side of the fjord
19.3.2013	16:12 – 16:18	73 – 1297	−44	Vertical profile down to the fjord head
19.3.2013	16:18 – 16:26	80 – 1436	+34	Profile up the glacier Mittag-Lefflerbreen
25.3.2013	14:15 – 15:53	25 – 972	−76 / +80	Saw-tooth pattern along the fjord

[a]A range (minimum–maximum) is given for profiles and the means with (minimum/maximum) deviations for horizontal flights. [b]Median flight aspect ratios of flight sections below 1 km a.s.l. (negative values for descent, positive for ascent).

to about 60 m during ascent or descent. All statistics were calculated using a moving window with 1 s time step (instead of the original 0.01 s, corresponding to 100 Hz resolution) along the flight path. Turbulent fluxes of sensible heat were calculated from the low-level horizontal flights. First, the wind components in each 2500-m bin were aligned to components along the mean wind and perpendicular to it (cross-wind, vertical wind) using the double-rotation method. Then, a linear trend was removed from the potential temperature and wind components, and a linear vertical gradient from the potential temperature, caused by flight altitude variations, was also removed. The turbulent sensible heat fluxes were calculated from the covariance of the potential temperature fluctuation and vertical wind component. Finally, mean quantities from all flights, such as mean wind speed (and direction), mean temperature and mean potential temperature, mean specific humidity, as well as turbulent statistics, that is, variances of wind velocity components and the TKE were calculated. Additionally, the Froude number was calculated as U/(NH), where U is the mean wind speed, N is the Brunt-Väisälä frequency and H is the vertical distance to the top of the mountain.

Measurements along each saw-tooth pattern were transformed into a two-dimensional (distance, height) cross-section along the fjord axis with a horizontal resolution of 100 m and a vertical resolution of 10 m. This was done by vertical filtering and then linear interpolation of the saw-tooth data in a horizontal direction. After the interpolation the lowest level data were extrapolated to the lowest available measurement altitude at about 40 m above the surface. Finally, the surface radiation temperature measurements were added as the surface boundary conditions for the temperature. We only used radiation temperature measurements collected from flight altitudes below 100 m to reduce the influence of atmospheric temperature. All aircraft measurements can be accessed at the PANGAEA data repository (Michaelis et al. 2023).

High-resolution atmospheric reanalysis products

The synoptic-scale weather conditions and the flow structures around Wijdefjorden were evaluated by applying the CARRA data set (Schyberg et al. 2020). CARRA was selected because of its small grid spacing—2.5 km—compared to 31 km in the ERA5 reanalysis. In a study focusing on a Norwegian fjord, Køltzow et al. (2022) found that CARRA outperforms the ERA5 reanalysis. The data set consists of 3-hourly analyses of atmospheric and surface meteorological variables on two different domains, the West domain and the East domain. Although both domains cover the study area (Wijdefjorden), we used the East domain, because it covers the entire Svalbard archipelago and its surrounding waters. We analysed the large-scale synoptic weather conditions based on pressure-level data of geopotential height, temperature and wind. The

small-scale flow structures were analysed using wind and temperature data from the second-lowest model level (level 64), which is approximately 34 m above the surface. Model-level data from levels 40 to 65 were used to analyse the flow features within the fjord. The lowest 20 levels (levels 46–65) are within the lowest 1 km above the sea surface of the fjord. In addition, reanalysis output for SIC, SST, snow on land, orography and the land–sea mask was used.

Sea-ice conditions in CARRA are described by the simple thermodynamic sea-ice scheme (Batrak et al. 2018), in which SIC or ice depth do not evolve in time. Initial conditions for SIC are obtained from two distinct products, as described in Yang et al. (2020). They are SICCI (Toudal Pedersen et al. 2017) and OSI-450 (Tonboe et al. 2016). The SICCI product is prioritized whenever available within a range of ±5 days and the OSI-450 product is used to fill data gaps. Both SICCI and OSI-450 data sets have a spatial resolution of 25 km, which is insufficient to capture ice conditions within narrow fjords, but in CARRA these SIC data are extrapolated along the coasts to provide data for fjords such as Wijdefjorden. For the SST input, the OSTIA (Donlon et al. 2012) data set is employed in CARRA. OSTIA offers a higher resolution of 0.05° so that SST fields exhibit fewer coastal issues compared to SIC data because of the utilization of higher resolution infrared observations. In CARRA, SST is used to correct SIC data. Namely, sea ice is removed where the SST exceeds a given threshold in either the ESA CCI's SST product or the Canadian Meteorological Centre's global SST products. This selection criterion is only applied to remove sea ice from locations where SST is above the freezing point and does not add SIC in the opposite scenario.

Results: environmental and synoptic-scale weather conditions during the flight missions

The ground surfaces were snow-covered on 17 March and the fjord's ice cover extended from the head of the fjord to about 72.5 km north of the fjord head, that is, the innermost (southernmost) part of the fjord, farthest from the open sea (Fig. 1d). The flights were performed during the daylight period, which lasted for approximately 11 hours. The low solar elevation angle (about 10°) and high albedo of the snow-covered surfaces made the effect of solar radiation on the surface energy balance small.

Synoptic conditions according to CARRA during the flights are shown in Fig. 2. On 19 March, when the main flight mission took place, there was a large low-pressure area south-west of Svalbard and a high-pressure area in the north-west. At 12:00 UTC (all times are UTC), the large-scale winds above the mountain tops (at 850 hPa pressure level) were east–north-easterly (Fig. 2b). Near the surface, winds north of the fjord were from the north-east and they channelled to northerly over the fjord (Fig. 3, Supplementary Fig. S1b, f). During the day, a ridge of high pressure strengthened from the north-west to the eastern parts of Svalbard. Therefore, winds above Wijdefjorden were easterly at 15:00 but changed to east–south-east by 18:00 (Supplementary Fig. S1c). This small change in the large-scale wind direction caused a weakening of the northerly channelled flow near the surface over the fjord by 18:00 (Supplementary Fig. S1g) The changes in near-surface wind field will be further discussed later in this article.

On 17 March, there was also a large low-pressure system south-west of Svalbard (Fig. 2a). A ridge of high pressure coming from the north-east to Svalbard moved

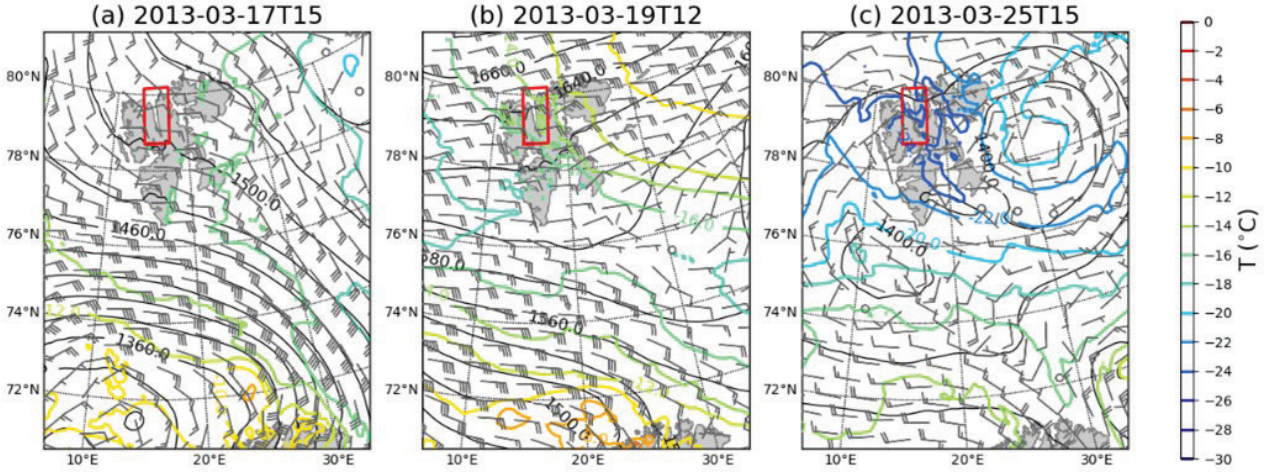

Fig. 2 CARRA 850 hPa pressure level geopotential height, temperature and wind on (a) 17 March 2013 at 15:00 UTC, (b) 19 March at 12:00 and (c) 25 March at 15:00. The Wijdefjorden region is highlighted by a red box.

Citation: *Polar Research* 2025, *44*, 9263, http://dx.doi.org/10.33265/polar.v44.9263

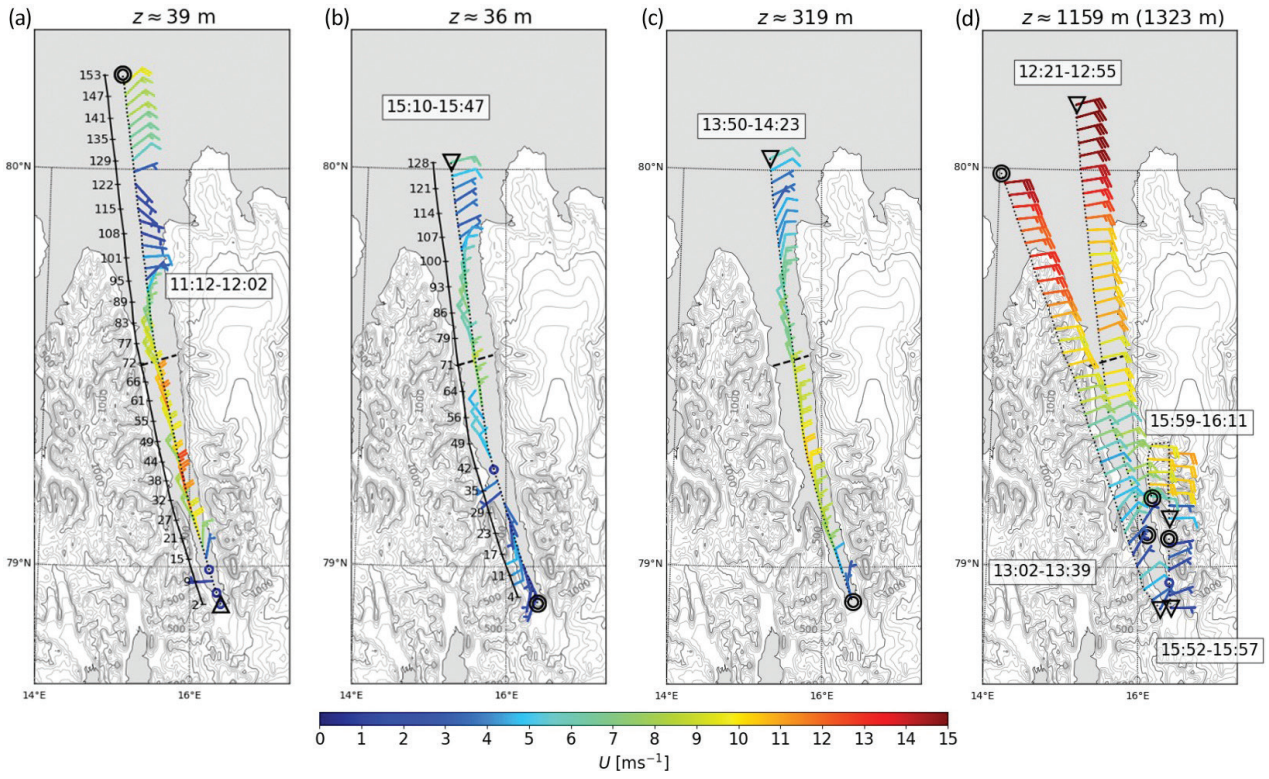

Fig. 3 Wind barbs from horizontal flights on 19 March 2013. The colour scale shows the speed of the horizontal wind. The sea-ice edge is marked by a dashed black line and the start and end points of flight legs are indicated by triangles and circles, respectively. The time (UTC) of the flight is given in a box next to each flight path. In (a) and (b), the distance (km) from the fjord head is shown next to the flight path, at intervals of 2 minutes of flight time. Topography is shown with 100 m contour intervals; bold contours represent isohypses of 500 m and 1000 m (Amante & Eakins 2009). The mean flight height is given above each panel. For (d), the value in parentheses is the height of the flight during 15:59–16:11; all other flights in (d) had a mean flight height close to 1159 m a.s.l. (see also Table 2).

during the day towards the north-west, over the archipelago, thereby turning the wind to easterly over Wijdefjorden by 15:00, when the saw-tooth pattern was flown (15:13–16:02). The near-surface winds were also easterly over the eastern side mountain ridge, but within Wijdefjorden the channelling of the wind was not as clear as on 19 March. On the western side of Wijdefjorden, the near-surface winds were weak and their direction was variable (Supplementary Fig. S1a, e).

The weather pattern on 25 March was very different compared to the other two days (Fig. 2c). There was a small low-pressure system with two centres, one east of Svalbard, the other one south-west of Svalbard. Wijdefjorden was located in the cold sector of the low-pressure system and the prevailing winds at 850 hPa level were mainly easterly or east–south-easterly at the time of the saw-tooth pattern flight (14:15–15:53). The near-surface winds were easterly north of Wijdefjorden and above the mountains east of the fjord, but it was almost calm near the surface over the fjord (Supplementary Fig. S1d, h).

In the following we focus on the results of the most extensive flight mission of 19 March, complemented by some comparisons with the conditions on 17 and 25 March.

Results: mesoscale and boundary-layer processes over the fjord

Channelling of the flow

On 19 March, the wind flow north of Wijdefjorden was east–north-easterly at all measurement heights (Fig. 3). But while the wind direction ranged from north-east to east–north-east along the whole horizontal tracks at 1159 and 1323 m a.s.l., the impact of topography is seen in the lower flight sections. Near the mouth of the fjord, in the wake region of the mountains on the eastern side, between 79.8 and 80°N, a relative minimum occurred in the wind speed near the surface and at the altitude of 319 m. Farther south, where the western side mountains are higher, the flow turned gradually to northerly, along the

fjord axis, at 319 m a.s.l. and below, clearly showing channelling. The same pattern can be seen from the distance–height cross-section of wind shown in Fig. 4a. North of the fjord, the profile of wind at about 150 km distance from the fjord head shows that the ABL reached about 500 m a.s.l. and the speed of the north-easterly wind within the ABL was approximately 10 m s^{-1}. Above the ABL the wind turned to a more east–north-easterly direction and accelerated. The cross-section of wind also confirms that east–north-easterly winds occurred between the surface and 1200 m a.s.l. close to the mouth region of the fjord, located some 100–130 km from the fjord head. But channelling occurred further south (Fig. 4a). Additional details and profiles can be found in Supplementary Fig. S2d–f.

On both sides of Wijdefjorden, the mountain height increases from the mouth region towards the south. The highest peaks on both sides exceed 1 km in height; on the eastern side they reach a bit higher than on the western side. The gradual turning of the wind to a northerly direction, along the fjord axis, followed the profile of the mountains on the fjord's western side up to an altitude of about 600 m. Above this level, the flow remained easterly from the mouth region to about 70 km north of the fjord head. The turning of the wind in the mouth region at 80–110 km from the fjord head coincided with a large TKE at all heights (Fig. 4b). Elevated values of TKE were observed also because of the unstable stratification over the open water in the northern parts of the fjord. The presence of a capping inversion layer at about 400–600 m a.s.l. between 30 and 85 km from the fjord head (Fig. 4c, d) resulted in high Brunt-Väisälä frequencies (N^2) and low Froude numbers (<1) in this area above 400 m. Apparently, the inversion layer acted as a barrier, preventing the well-mixed air mass near the surface from flowing over the western side mountain range. The mountains, supported by the stratification of the air mass, created a barrier wind, seen as flow channelling and formation of an LLJ over the fjord.

Main flow characteristics over the fjord

In addition to channelling, there were further important characteristics of the flow over the fjord (Fig 4, Supplementary Fig. S2d–f). These characteristics are closely connected to the temperature structure, which, in turn, is a consequence of two primary factors: first, the transition from warm open water to cold sea ice in the middle of the fjord; and, second, the channelling of the wind that generated an on-ice flow, orthogonal to the ice edge. The potential temperatures in Fig. 4a show four different regimes. (i) In the mouth region, there was a cold convective boundary layer over the open ocean, which (ii) became warmer when the flow approached the sea-ice edge. (iii) South of the ice edge, over the cold sea-ice surface, a stable stratification developed from the surface. Finally, (iv) the northerly channelled flow met a cold-air pool in the south. We discuss these regimes in more detail below.

Over the open water, from the ice edge to 110 km distance from the fjord head, the upward sensible heat fluxes were mostly within 28–108 W m^{-2} (based on horizontal low-level flights). This drove the mixing and heating in the ABL up to about 500 m a.s.l. From the surface to a height of 250 m, temperatures increased by up to 1.2 K along the fjord axis from the mouth region to the ice edge.

The temperature structure downstream of the sea-ice edge in regimes iii-iv can be explained by the cooling over the sea-ice surface and advection of the warmer air from regime ii over open water. The development is very similar to that obtained by Vihma et al. (2003; see their figures 3, 4) for an event of on-ice flow south-east of Svalbard, where the ABL was gradually cooling over ice while the ABL depth was increasing along the airmass trajectory. However, the development of the wind field in the fjord differs from the simple flow without orography and without convection on the upwind side of the ice edge described by Vihma et al. (2003). In our case, also the wind field reflects the four different regimes, which are visible in the temperature field. First, over the open water in regime i north of the ice edge, the vertical profile of wind speed was relatively uniform, as expected in a convective boundary layer. When approaching the ice edge in regime ii, the wind accelerated because of the combined effects of stratification and orography. In the stable internal boundary layer developing near the surface south of the ice edge, the stable stratification reduced the friction (Brümmer & Thiemann 2002), and thus further increased the ABL wind speed in regime iii. A well-defined LLJ was formed here in the middle of the fjord, bounded by stable layers from above and below, and laterally constrained by the orography. The vertical structure of the wind profile resembled that of gap flows (Flamant et al. 2002). Finally, in the region (regime iv) of the cold-air pool, the wind speed decreased markedly near the surface.

The ABL wind speed maximum (Fig. 4b–d) follows closely the region of low N^2 and high (>1) Froude numbers. In the middle of the fjord, this layer became shallower both from above and below. Above it, the height of the capping inversion decreased towards the south, especially over the open water between the ice edge and the point 110 km north of the fjord head (N^2 in Fig. 4c). Below the LLJ, the largest changes were found downwind of the ice edge, where the stable internal boundary layer formed.

Citation: *Polar Research* 2025, *44*, 9263, http://dx.doi.org/10.33265/polar.v44.9263

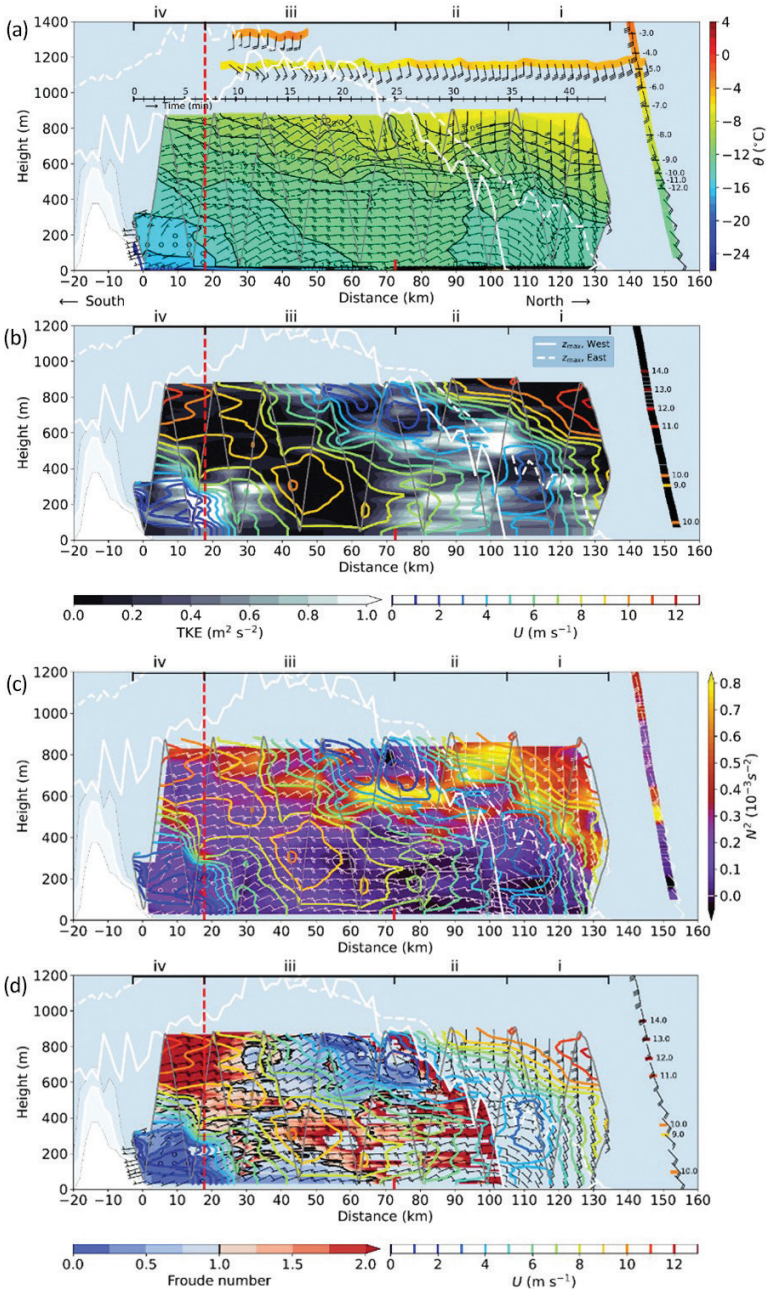

Fig. 4 (a) Potential temperature and wind vectors based on the saw-tooth pattern flight on 19 March 2013 (pale grey saw-tooth line superimposed on the colour scale, 14:25–15:10 UTC) along the fjord, two horizontal flights at about 1200–1300 m a.s.l. (12:20–12:55, 15:58–16:11; see Table 2) and a profile north of the fjord during 12:05–12:14 on 19 March. Upward/downward directions of the wind barbs indicate easterly/westerly wind directions, and southerly/northerly winds are from left/right; location of the ice edge (defined on the basis of horizontal low-level flights) is shown by a red line at a distance of 72.5 km. The time axis of the saw-tooth pattern flight is shown by the horizontal line above the flight pattern, where bins are shown at 1-minute intervals starting from the beginning of the flight at the fjord head. In (b), TKE is shown on a black/white scale and horizontal wind speed as coloured contours. (c) The Brunt-Väisälä frequency squared (N^2) and (d) the Froude number relative to the height of the mountains on the western side. Panels (c) and (d) also include the wind barbs and the speed of the horizontal wind as coloured contours. In all panels, the location of the front of the cold-air mass is indicated by a red vertical dashed line, and the maximum terrain elevations of the mountains on the eastern/western side of the fjord are shown by white dashed/solid lines. The minimum, median and maximum height of the mountains south of the fjord are shown in white at negative distances. The vertical dashed red line marks the position of the front of the cold-air mass with southerly flow. Different flow regimes, i–iv, are indicated at the top of each panel.

Next, we compare the effects of orography and stratification. The narrowing of the fjord towards the south (Fig. 1c, Supplementary Fig. S4) supported the wind acceleration. The average width of the fjord below 500 m a.s.l. decreased by 5.6 km from 80 km to 40 km from the fjord head (Supplementary Fig. S4), corresponding to a 32% change in cross-sectional area. A similar change in the cross-sectional area would be obtained by a 160 m decrease in the ABL depth in the case of a constant fjord width. The cross-sections in Fig. 4c, d show rather patchy patterns of the Froude number, but two features are obvious. First, one can see an inclined band of high Froude numbers, touching the surface near 80 km distance and being clearly elevated from the surface by about 200 m at 40 km distance. Second, the top of the layer first decreased from about 600 m at 80 km distance to 500 m at 60 km distance and then increased farther south. Altogether, this indicates a depth change of the layer with high Froude numbers by about 300 m, which is more than the 160 m change attributed to orography. This reveals that the stratification also had a remarkable impact, potentially comparable to, or even larger than, the influence of orography. However, it is important to note that the orography also affects the Froude number, that is, our interpretation of the stability effect. Furthermore, unlike orography, inversion layers or layers with below-one Froude numbers are not "solid" boundaries. Overall, we can conclude that both orography and stratification played crucial roles in the wind acceleration.

As mentioned above, in the southern parts of the fjord, the northerly channelled flow encountered a pool of cold air. The Froude number within the cold-air pool was clearly below one (Fig. 4d), while within the LLJ it exceeded one. Consequently, the northerly flow—being more buoyant than the air in the cold-air pool—was forced to rise above the cold near-surface layer. This interaction not only increased the height of the LLJ but was probably the main reason for an acceleration of the LLJ in the southern parts of the fjord (Fig. 4d). The maximum speed of the LLJ observed along the saw-tooth pattern was 11.5 m s^{-1} at 817 m a.s.l. at 7.2 km distance from the fjord head. This maximum was observed clearly above the highest mountains south of the fjord, that is, the flow continued over the mountains in the upper parts of the profile. But near the surface, within the cold-air pool, a shallow layer with southerly winds was observed over the sea ice and on the slope south of the fjord (Fig. 4a, d).

The formation of a cold-air pool typically arises from surface radiative cooling and the sinking of cold air from the surrounding mountain slopes due to gravity-driven drainage flows or katabatic winds. However, investigating when and how the cold-air pool was originally formed cannot be done on the basis of the data in this study. Instead, the next two sections will focus on the temporal changes in the structure of the cold-air pool during the flight day.

Front between warm and cold-air masses

A detailed consideration of the cold-air pool in the region south of 20 km distance from the fjord head (Fig. 4a) reveals some insight into small-scale processes and their variability in the fjord. Below about 80–120 m a.s.l., the flow direction was southerly in this region, that is, against the channelled northerly flow. On the basis of the saw-tooth pattern flight shown in Fig. 4a, it can be determined that the front between the cold southerly (the cold-air pool) and warm northerly air masses was located at about 18 km distance from the fjord head. There, both the wind direction and temperature changed and TKE showed a maximum. This front location is, however, only a rough estimate that is based on linearly interpolated fields of potential temperature, wind and TKE.

A more reliable detection of the front location is possible based on the two low-level horizontal sections flown along the fjord before noon, almost 2.5 hours before the saw-tooth flight, and in the afternoon, right after the saw-tooth pattern (Table 2, Fig. 5). The front was determined here as the location with the largest horizontal potential temperature gradient (vertical black line), so that it can be called a thermodynamic front, as done by Atkins et al. (1995). Close to it, a peak in TKE was observed. Another front, namely a kinematic front (Atkins et al. 1995), was observed as well. It is characterized by a change in the wind direction from southerly to northerly. Its determination based on the horizontal wind gradient results in a position 2.0 km south of the thermodynamic front (not shown in Fig. 5a).

In the afternoon, the thermodynamic front was located about 44.3 km north of the fjord head (Fig. 5b) while a calculation of the wind gradient showed the kinematic front position at about 1.6 km south of the thermodynamic front position. Again, a peak in TKE and in the gradient of the northerly wind velocity occurred just behind the location of the thermodynamic front. To summarize, the thermodynamic front moved some 28 km northward during the 4.3-hour period from before noon to afternoon. At low levels the distance between the thermodynamic front and the kinematic front decreased slightly, from 2.0 km at noon to 1.6 km in the afternoon.

The northward propagation of the front was accompanied by temporal changes observed in the ABL in the southern parts of the fjord (Fig. 5). Air potential temperatures along the glacier were similar before noon and in the afternoon, but in the afternoon the minimum surface potential temperatures decreased from around −23°C

Citation: *Polar Research* 2025, *44*, 9263, http://dx.doi.org/10.33265/polar.v44.9263

to minima below –25°C (at -15 km, i.e., south-east of the fjord head). This change went along with a change in the flow over the glacier from westerly (cross-slope direction) before noon to southerly (downslope) by the afternoon. The cold surface temperatures in the middle parts of the slope probably contributed to the formation of the southerly drainage flows in the afternoon and thus also to the further propagation of the cold-air mass front.

This propagation was not linear (Table 3). At first, the front propagated only about 2 km between 11:16 and 14:32 (in 3.25 hours) and then between 14:32 and 15:34 about 26 km per hour. The southerly winds near the surface in the core of the cold-air pool were mostly weak, below 5 m s^{-1} (less than 18 km per hour). Therefore, the fast propagation of the front in the afternoon cannot be explained by the northward advection of the cold-air mass from the head of the fjord only, but parts of the cold-air mass must have originated from the slopes on the sides of the fjord. Terrain-following flights were only available from the slopes of the Mittag-Lefflerbreen glacier south-east of the fjord head. However, it is highly probable that lower surface potential temperatures caused by radiative cooling also occurred elsewhere over the surrounding snow-covered mountains, changing the downslope flow elsewhere in the southern parts of the fjord. This is supported by observations at about 35 km north from the fjord head, where Vestfjorden is located (see also wind barbs in Fig. 3b). There, the flow direction was from the south-west, that is, along the axis of Vestfjorden.

Table 3 Location and the timing of the thermodynamic (kinematic) front of the southerly cold-air mass.

Time (UTC)	Distance (km)	Flight pattern
11:16	16.0 (14.0)	Horizontal flight
14:32	18	Saw-tooth
15:34	44.3 (42.7)	Horizontal flight

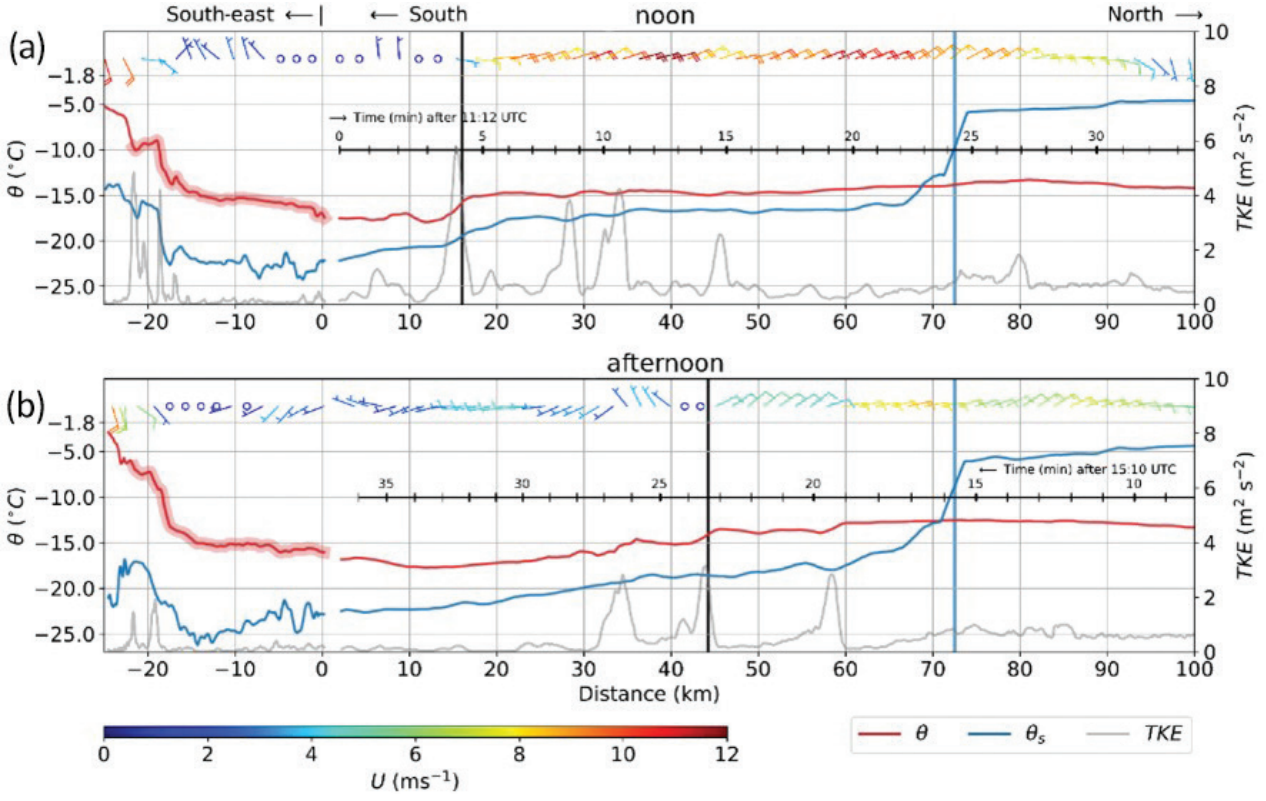

Fig. 5 Potential temperature (red lines), surface potential temperature (blue lines), wind barbs and TKE (grey, on the right-hand axis) based on low-level horizontal flights and flights following the terrain of the glacier Mittag-Lefflerbreen (at negative distances) on 19 March 2013 (a) near noon and (b) in the afternoon. Time (since the beginning of the horizontal low-level flight leg) is shown as a horizontal black line with tick marks at each 1-minute interval. Flight direction is shown by the arrow next to the time axis label. The location of the front of the southerly cold-air mass is marked by a vertical black line and the ice edge by a vertical light blue line. The wind direction shown by the wind barbs: from right/left indicates northerly/southerly and upwards/downwards indicates easterly/westerly winds. The section of the glacier flights where the flight height above the local surface was less than 100 m is highlighted in both panels by a red shading.

Flow over the fjord head region

The small-scale spatial variability of the flow is evident especially in the fjord head region. As a qualitative illustration, Fig. 6 shows the saw-tooth pattern flight in the afternoon and the profiles over the Mittag-Lefflerbreen glacier at noon and in the afternoon, whereas Fig. 7 presents separate profiles of the noon and afternoon conditions. The flow field in the fjord head region can be roughly divided into four regimes: (1) the large-scale easterly flow above the mountain tops (yellow arrows and level A); (2) the channelled northerly flow over the fjord (red arrows, levels B and C over the fjord head); and (3) westerly cross-slope flow over the glacier near noon (blue profile, altitudes below 650 m, including level C); and (4) southerly winds within the cold-air pool near the surface at the fjord head and over the lowest parts of the glacier slope in the afternoon (cyan arrows near the surface).

At noon, all four wind regimes can be identified in Fig. 8a. In the upper parts of the profiles, above 1100–1200 m a.s.l., a large-scale east–north-easterly flow prevailed (first regime). The east–north-easterly winds were stronger over the glacier south-east of the fjord (Fig. 8c, blue profile) than above the fjord head (green profiles). Over the fjord head, northerly winds (second regime) extend from approximately 100 to 1100 m a.s.l., including levels B and C. The winds between B and C represent the LLJ generated by the wind channeling along the fjord. The maximum wind speed within the LLJ was 13.2 m s^{-1} at 573 m a.s.l. (light green profile in Fig. 8c), just above the average height of the mountains to the south of the fjord head (above level C). In addition, northerly winds were observed in a shallow layer at level B in the upper sections of the Mittag-Lefflerbreen glacier (blue profile in Fig. 8a, c), located south-east of the fjord head.

The third wind regime in Fig. 8a, south-westerly winds, was observed below 650 m a.s.l. at noon. The airflow was cross-slope over a large part of the slope and turned to downslope only very close to the fjord head, below 100 m a.s.l. These southerly winds in the fourth wind regime were observed at noon only locally in a shallow layer close to the fjord head.

The profiles over the southern parts of the fjord before noon and in the afternoon show temporal changes in the boundary-layer structure. The primary differences between the noon and afternoon cases refer to changes in the strength and depth of the LLJ and to an increase in the depth of the cold-air pool. The maximum speed of the LLJ decreased from noon (Fig. 8c, green profiles) to afternoon (orange and red profiles), and its peak height was observed at a higher elevation, near level B in the afternoon (orange and red profiles), whereas near noon it was closer to level C. In the cold-air pool, the flow was

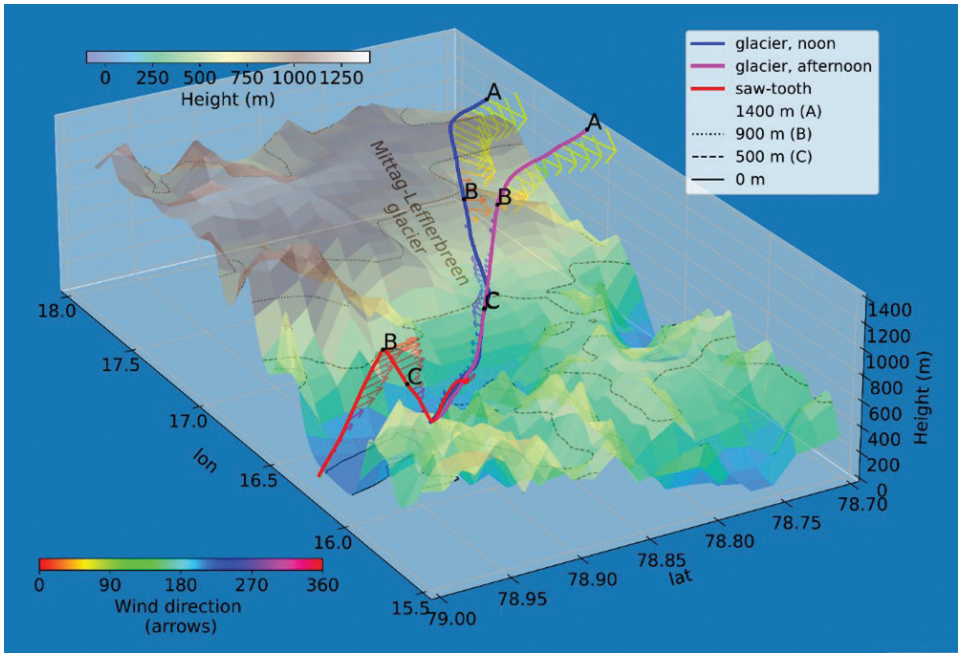

Fig. 6 A three-dimensional illustration of the orography at the fjord head region and wind profiles based on the saw-tooth pattern (red profile) and two flights over the glacier Mittag-Lefflerbreen south-east from the fjord head (blue profile, noon; magenta profile, afternoon). Arrow colours represent wind direction and points A, B and C along each profile indicate altitudes of 1400, 900 and 500 m a.s.l., respectively.

Citation: *Polar Research* 2025, *44*, 9263, http://dx.doi.org/10.33265/polar.v44.9263

characterized by southerly winds (cyan barbs in Fig. 8a, b). The depth of the layer with southerly winds increased from 50 to 80 m before noon (Fig. 8a, green profiles) to about 80–120 m during the saw-tooth pattern flight (Fig. 8b, the first red profile, "N") and up to 180–220 m in the afternoon (orange profile in Fig. 8b). Additionally, southerly winds were also observed over the slope of the Mittag-Lefflerbreen glacier up to an altitude of approximately 550 m (at flight heights approximately 50 m above the local surface). Above this level, the winds over the glacier were mostly calm up to about 900 m a.s.l., where a small signal of north-easterly winds (orange barbs) was observed.

To summarize, the boundary-layer structure over the slope of the Mittag-Lefflerbreen glacier was complicated, with several inversion layers, layers with different wind directions, layers with enhanced turbulence (Fig. 8, Supplementary Fig. S5) and high temporal variability. At noon, the flow over the lower half of the glacier was not downslope but cross-slope (south-westerly), and it turned downslope only very close to the fjord head. When the northerly channelled flow weakened in the afternoon, the winds in the lowest parts of the glacier turned to southerly, that is, down the glacier (Fig. 8b), and contributed to the deepening of the cold-air pool in the southern parts of the fjord.

Differences between the three flight missions

So far, we have discussed the most comprehensive flight mission on 19 March, when several flight patterns were flown (Table 2). On 17 and 25 March, only a saw-tooth pattern was flown, but these flights allow us to compare the conditions in the fjord during the three days. The sea-ice conditions remained almost the same. Based on the surface radiation temperature measurements, the ice edge was located at about 72.5 km north of the fjord head on 17 and 19 March, whereas on 25 March it was a couple of kilometres closer to the fjord head.

On 17 March (Fig. 9), the potential temperatures were, overall, somewhat higher than on 19 March (Fig. 4). Over the sea ice there was a strongly stable layer

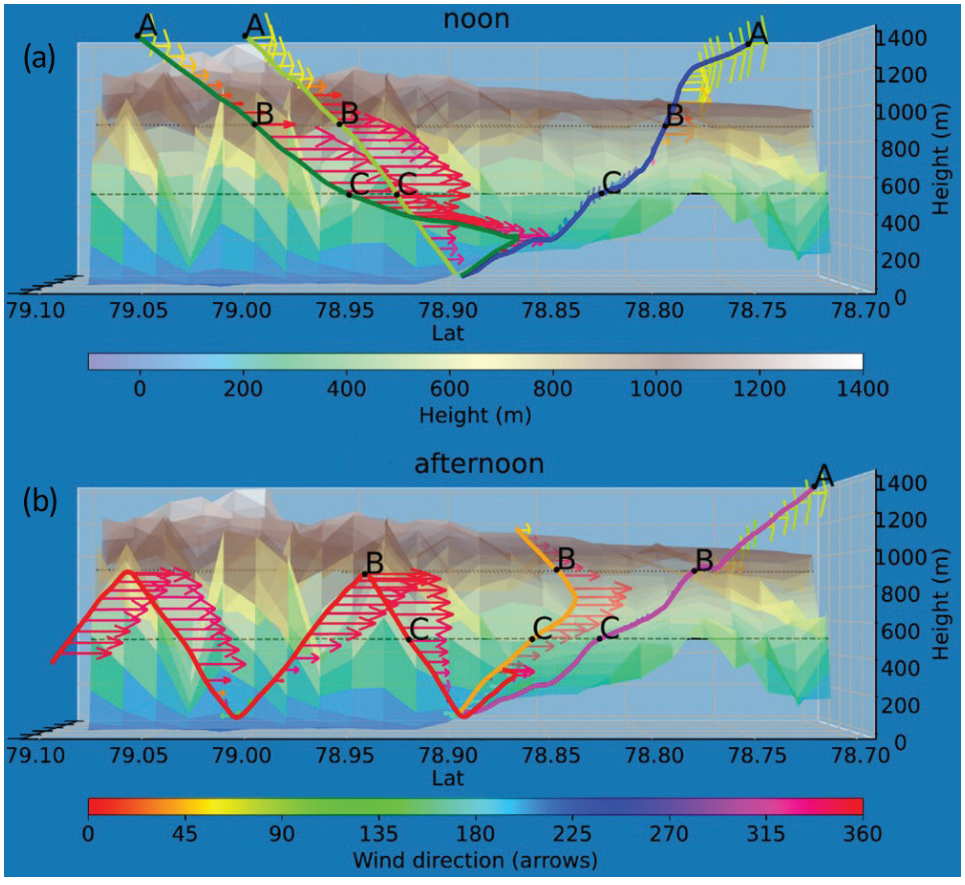

Fig. 7 Orography on the eastern side of the fjord and wind profiles (a) at noon and (b) in the afternoon. The view is from the west. Arrow colours represent wind direction. Points A, B and C indicate altitudes 1400, 900 and 500 m a.s.l., respectively, as in Fig. 6.

near the surface below 200 m a.s.l., where large positive N^2 values were observed (Fig. 9c). Within this layer, weak to moderate southerly winds were observed, which transported the cold air northwards to over the open water. On 17 March, channelling was observed only in the middle of the fjord around the ice edge region, where, in contrast to the 19 March conditions, the large-scale easterly winds turned to southerly. The channelling supported the thermally-driven near-surface southerly winds across the ice edge that transported cold air from over the sea ice towards the open water. The Froude number was small within most of the fjord, exceeding one only close to the mountain tops, where the flow was easterly (cross-fjord) (Fig. 9d). TKE within the fjord was mainly low, with highest values over the open water near the mouth of the fjord (Fig. 9b).

On 25 March, the overall potential temperatures were noticeably lower compared to the other two days (Fig. 10). As on 17 March, there was a cold stable layer (with large N^2) near the surface over the sea ice, and weak southerly winds were observed in a shallow layer across the sea-ice edge. On 25 March, the easterly flow north of the fjord channelled to northerly within the fjord, but only above approximately 200 m a.s.l. Along the flight path, at 73.2 km north of the fjord head, the maximum speed of the northerly wind, 1.9 m s^{-1}, was observed at an altitude of 212 m a.s.l. (Fig. 10). Downwind from the ice edge, the northerly flow accelerated and formed an LLJ, as on 19 March. The height of the LLJ increased towards the south. At a distance of 54.1 km from the fjord head, a maximum speed of 3.6 m s^{-1} was observed at an altitude of 450 m, and at a distance of 8.6 km a maximum of 5.9 m s^{-1} was observed at an altitude of 670 m a.s.l., which is above the mountain tops south of the fjord. The Froude numbers were small within the fjord, which supported the channelling of the wind (Fig. 10d). In the southern parts of the fjord above approximately 500 m a.s.l., the Froude numbers were above one, which also indicated that the LLJ extended over the mountains south of the fjord as a gap flow and probably reached Isfjorden in the south, as on 19 March.

Evaluation of the CARRA reanalysis data set

The CARRA data set aims to represent the atmospheric conditions in the Arctic. The research aircraft data set provides opportunities to evaluate the performance of CARRA in an Arctic fjord during three days in conditions where the large-scale flow at the height of the mountain tops is easterly but the flow field within the fjord differs between the days. Evaluating CARRA data against two-dimensional distance-height cross-sections of potential temperature and wind at the time of the saw-tooth pattern flights on 17, 19 and 25 March revealed that the most dramatic differences between the reanalysis and the observations occur over the sea-ice covered southern

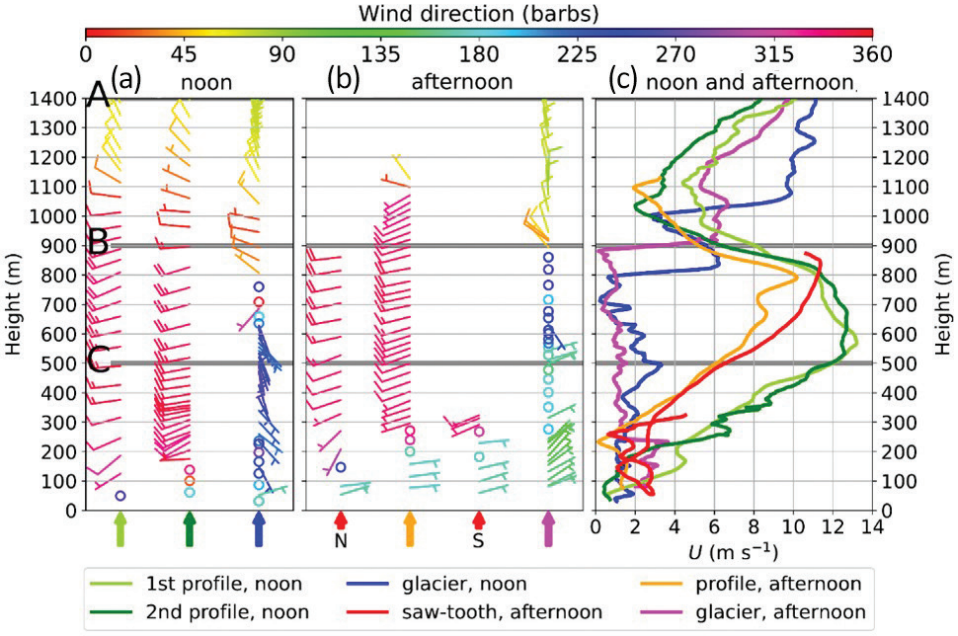

Fig. 8 Wind barbs (a) at noon and (b) in the afternoon, and (c) the horizontal wind speed both at noon and in the afternoon. Arrows below each wind barb profile in (a) and (b), and the different colours in (c), refer to the colours in the legend below the panels. Location of profiles in the north–south direction is shown in Fig. 7. Wind barb colours represent wind direction. Horizontal grey lines indicate levels A, B and C, also shown in Figs. 6 and 7.

Citation: *Polar Research* 2025, *44*, 9263, http://dx.doi.org/10.33265/polar.v44.9263

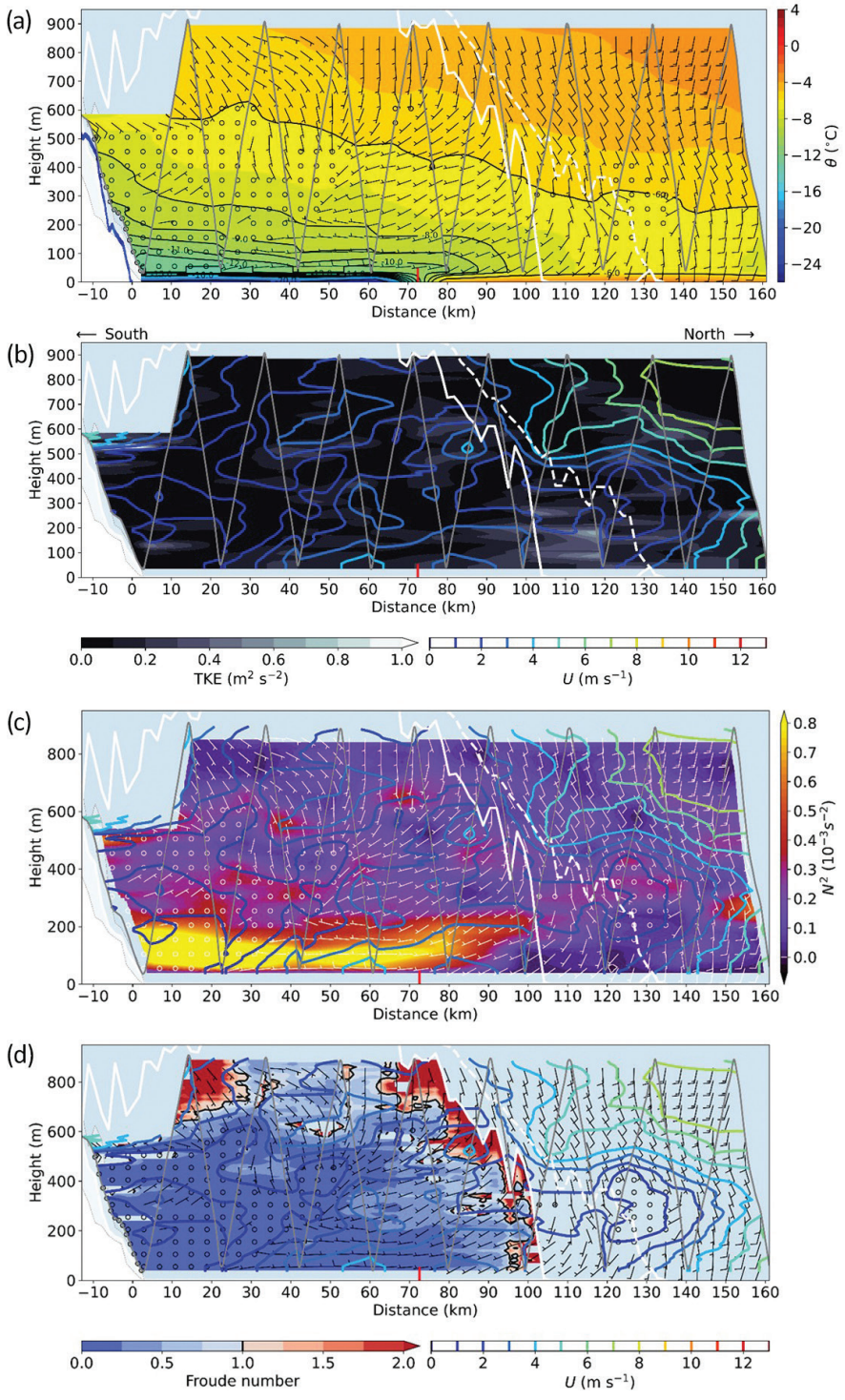

Fig. 9 (a) Potential temperature and wind vectors based on the saw-tooth pattern flight on 17 March 2013 (grey line at the top of the colour scale, 15:13–16:02 UTC) along the fjord. Upward/downward directions of the wind barbs indicate easterly/westerly wind directions, and southerly/northerly winds are from left/right; location of the ice edge is shown by a red line at a distance of 72.5 km. In (b), TKE is shown on a black/white scale and horizontal wind speed as coloured contours. (c) The Brunt-Väisälä frequency squared (N^2) and (d) the Froude number relative to the height of the western side mountains. Panels (c) and (d) also include the wind barbs and the speed of the horizontal wind as coloured contours. In all panels, the maximum terrain elevations on the eastern/western side of the fjord are shown by white dashed/solid lines, respectively. The minimum, median and maximum height of the mountains south of the fjord are shown in white at negative distances.

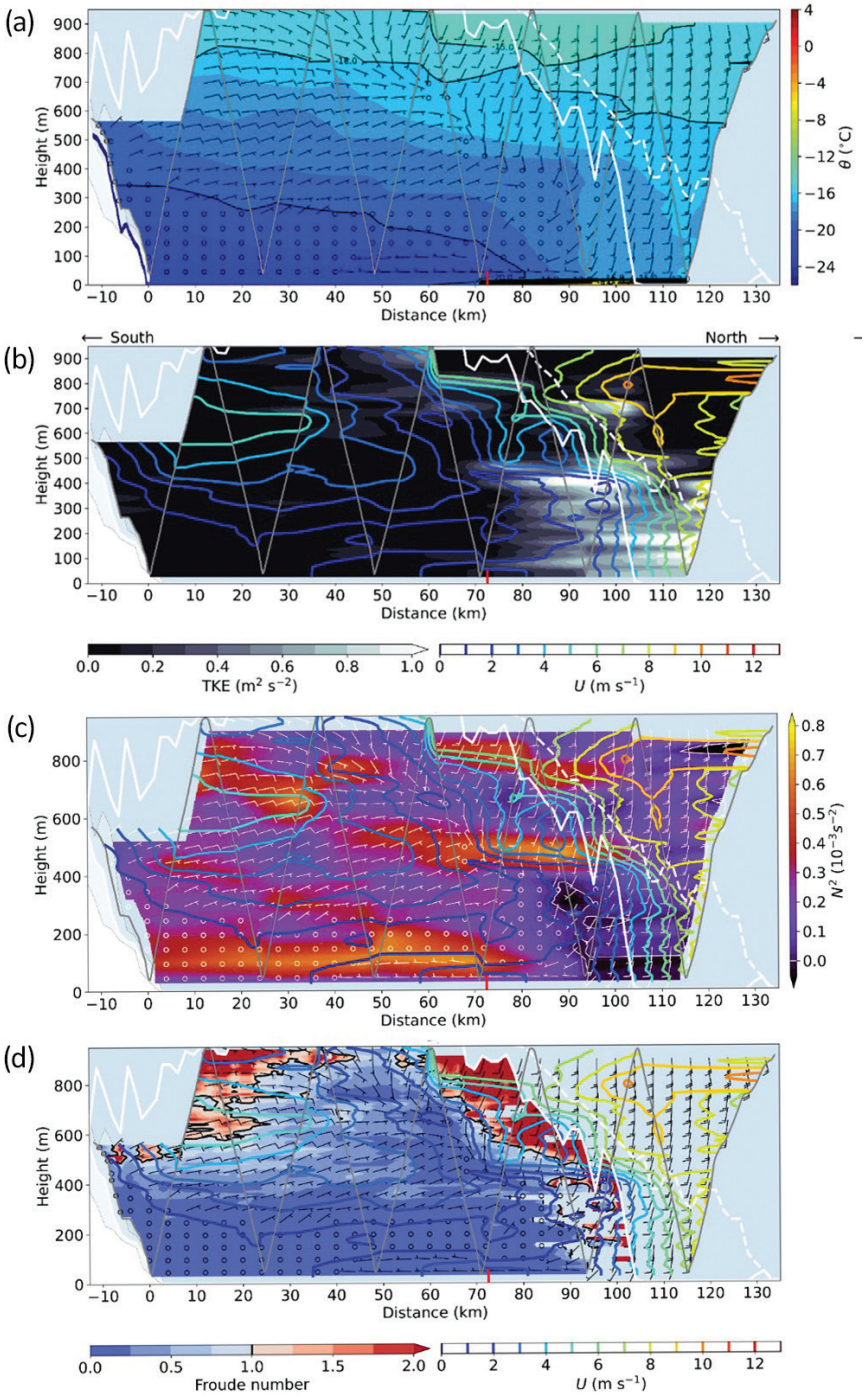

Fig. 10 (a) Potential temperature and wind vectors based on the saw-tooth pattern flight on 25 March 2013 (grey line at the top of the colour scale, 14:15–15:53 UTC) along the fjord. Upward/downward directions of the wind barbs indicate easterly/westerly wind directions, and southerly/northerly winds are from left/right; location of the ice edge is shown by a red line at a distance of 72.5 km. In (b), TKE is shown on a black/white scale and horizontal wind speed as colored contours. (c) The Brunt-Väisälä frequency squared (N^2) and (d) the Froude number relative to the height of the western side mountains. Panels (c) and (d) also include the wind barbs and the speed of the horizontal wind as coloured contours. In all panels, the maximum terrain elevations on the eastern/western side of the fjord are shown by white dashed/solid lines. The minimum, median and maximum height of the mountains south of the fjord are shown in white at negative distances.

Citation: *Polar Research* 2025, *44*, 9263, http://dx.doi.org/10.33265/polar.v44.9263

parts of the fjord. In CARRA, Wijdefjorden was practically ice free, except for a few coastal grid points on the eastern side of the fjord at about 30–55 km from the fjord head. Those grid points were probably caused by land-to-ocean spillovers, which are open water pixels classified as ice in the proximity of land. The SIC data in CARRA were based on the ESA CCI SIC. Because of its coarse resolution of 25 km, the SIC data in the fjord were obtained by extrapolating from the nearest data point north of the fjord, which was ice free (SIC = 0).

The absence of sea ice in the reanalysis resulted in a warm bias over the southern parts of the fjord, influencing the flow patterns within the fjord. None of the days exhibited near-surface southerly flow in the reanalysis in the southern half of the fjord (Fig. 11, Supplementary Figs. S6, S7). On 17 March, the wind field north of 70 km from the fjord head closely resembled the observed wind field (Supplementary Fig. S6), suggesting that the observed southerly winds north of the ice edge were caused not only by the horizontal temperature gradient across the ice edge but also by the orographic channelling within the fjord. However, north of the fjord, particularly above 500 m altitude, the winds in CARRA were weaker compared to the observations.

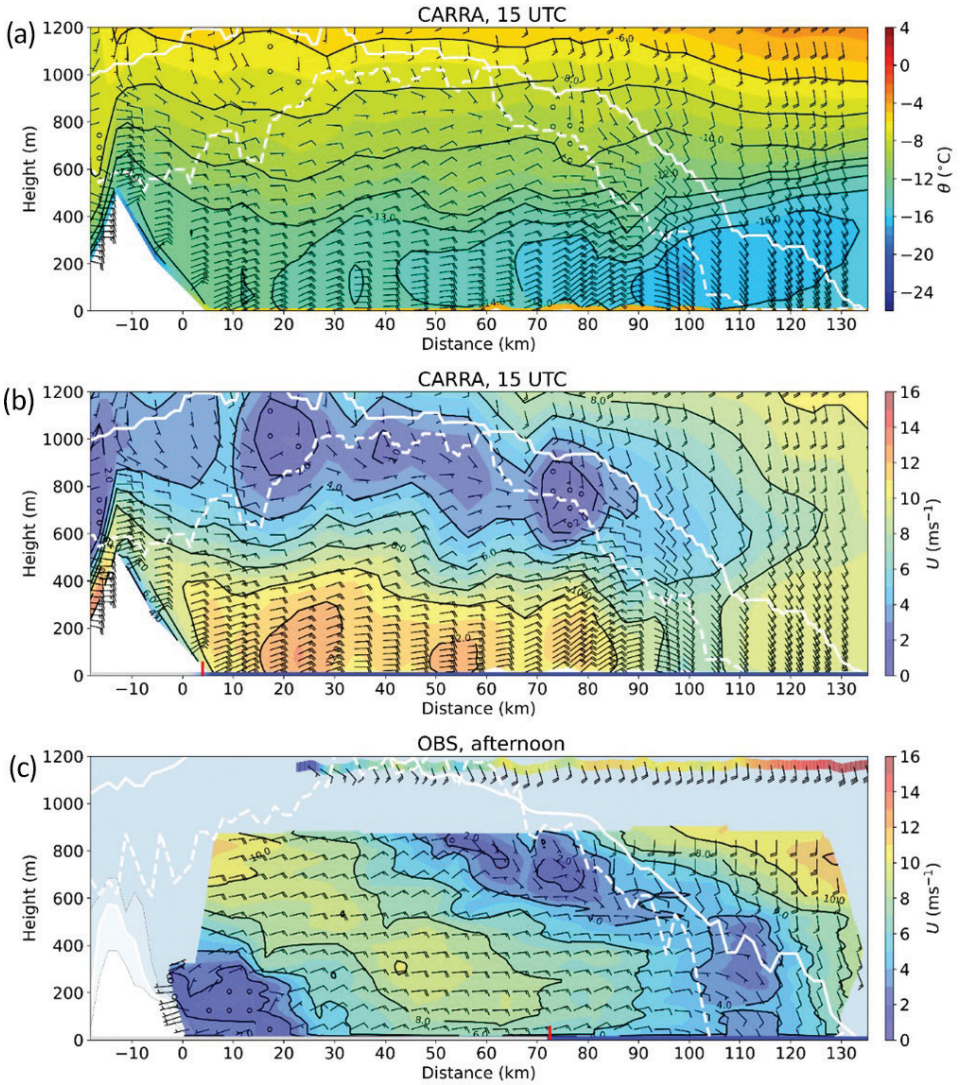

Fig. 11 Distance–height cross-sections of (a) potential temperature and (b, c) wind speed and (a–c) wind barbs based on (a, b) CARRA reanalyses on 19 March 2013 at 15:00 UTC and (c) observations. Panel (c) includes results from the saw-tooth pattern, the flight up the glacier (16:18–16:26) and two horizontal flights, as in Fig. 3a. The surface type—ice/snow (grey) or water (blue)—is shown by the horizontal line at the bottom of (b) and (c). Maximum terrain elevations of the mountains on the eastern/western side of the fjord are shown by solid/dashed white lines. In (a) and (b) they were derived from CARRA; in (c) from Amante & Eakins (2009).

On 25 March, the CARRA potential temperatures within the fjord were generally higher than observed. In CARRA, the lowest temperatures occurred over the glacier in the south, whereas the observed cold-air pool extended over the sea ice up to approximately 70 km north of the fjord head and even beyond. Despite this difference, there was some wind channelling to a northerly direction within the fjord in CARRA, but the channelling reached down to the surface, whereas in reality it only occurred above 200 m a.s.l. Furthermore, in CARRA the maximum speed of the LLJ caused by the channelling was weaker than observed, and the southerly flow near the surface in the middle of the fjord was not captured by the reanalysis at all (Supplementary Fig. S7).

On 19 March, the lowest near-surface potential temperatures in CARRA were found at the mouth of the fjord (Fig. 11a) whereas the observed ones occurred at the fjord head (Fig. 4a). However, CARRA reproduced the warming of the near surface air north of 70 km, although the absolute values of the potential temperature were lower than observed. North of the ice edge, the observed SST based on surface radiation temperature measurements was close to the SST of CARRA, but over the sea ice the observed surface temperatures were much colder than the SST of the reanalysis. The reanalysis generates channelling of the wind in the fjord (Fig. 11b); however, the maxima of the LLJ are too strong and found only below 300 m throughout the fjord, whereas the observed height of the LLJ maximum increased towards the fjord head as the northerly channelled flow rose above the cold-air pool close to the fjord head. As CARRA does not realistically represent the cold-air pool in the southern parts of the fjord, the bias in the near-surface wind speed is large, as seen near the fjord head in Fig. 11.

In the southern parts of the fjord, there was a clear change in the near-surface flow pattern between the noon and afternoon of 19 March (Fig. 12a). At noon, the channelled flow reached 16.0 km north of the fjord head, whereas in the afternoon it was observed only north of 44.3 km from the fjord head. Further, in the afternoon, the winds south of 44.3 km were mostly opposite to the winds near noon. These dramatic changes observed in the wind must be due to temporal evolution of the flow field instead of spatial variability because the near-surface flights took place in locations close to each other (Fig. 12a). CARRA results also show temporal evolution in the wind field (Fig. 12b, c), although the changes were not as dramatic as observed. CARRA reproduced the channelling of the wind within Wijdefjorden and weakening of the channelled northerly wind in the afternoon, especially between 15:00 and 18:00, but, because of the lack of sea ice, it did not reproduce any southerly flow.

The CARRA-based results show that the large-scale distributions of potential temperature and wind were reproduced at higher altitudes above the fjord. In all three cases the flow was easterly both in observations and in the reanalysis. The speed of this easterly flow was somewhat underestimated in the upper parts of the cross-section north of the fjord in all three cases. The largest differences between the reanalysis and the observations were found within the fjord. The lack of sea ice in CARRA prevented the formation of the cold-air pool in the southern parts of the fjord.

Although CARRA did not reproduce the cold-air pool within the fjord, it captured the formation of the stable boundary layer and the katabatic flow over the mountains on the afternoon of 19 March (Fig. 13). Supplementary Fig. S8 shows the evolution of the temperature and wind profiles at about 5 km south of the fjord head, where the slope height was about 230 m a.s.l. in the model. At 12:00, the channelled northerly flow was strong, with a maximum speed of about 13.5 m s^{-1}. This LLJ in CARRA was as strong as observed before noon but its height was much lower, only about 80 m a.g.l. (310 m a.s.l.), whereas the observed maximum was close to 600 m a.s.l. In CARRA, this resulted in a low Richardsson number (Ri = 0.01) between the LLJ core height and the surface, that is, the conditions were close to neutral. When the channelled flow started to weaken in the model after 12:00, a surface-based inversion deepened over the slope, and the height of the LLJ increased. At 15:00, the core of the LLJ occurred at approximately 260 m a.g.l. (490 m a.s.l.), and Ri was about 0.2. Yet, contrary to the data from the saw-tooth flight pattern at 14:25, the CARRA near-surface wind did not turn downslope. By 18:00, the channelled northerly flow—the LLJ—had decreased further in CARRA to about 4.4 m s^{-1} over the slope (Fig. S8), and its core occurred at about 300 m a.g.l. (530 m a.s.l.). The surface-based inversion extended across the LLJ core, and southerly downslope winds were observed near the surface as another LLJ reaching about 100 m a.g.l. In other words, CARRA was able to reproduce the formation of the stable boundary layer over the slope and the resulting downslope flow once the TKE production by wind shear became weak enough, but it occurred later than observed.

Discussion

We have analysed the structure of the ABL in an Arctic fjord based on research aircraft flights during three days. Among the flow features studied, wind channelling is a common feature in Arctic fjords (Beine et al. 2001;

Citation: *Polar Research* 2025, *44*, 9263, http://dx.doi.org/10.33265/polar.v44.9263

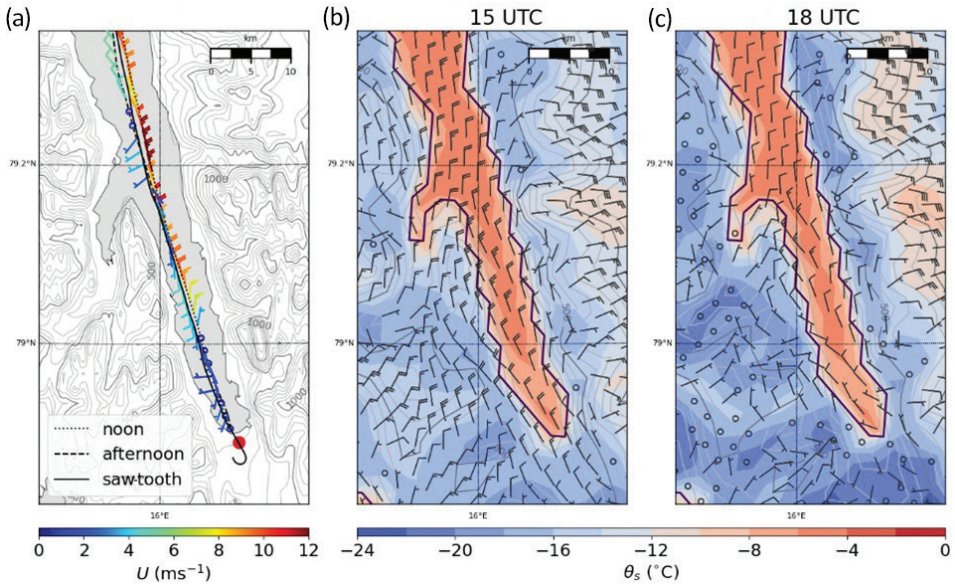

Fig. 12 (a) Wind barbs from the two low-level horizontal flights along the fjord axis on 19 March 2013 during 11:12–12:03 UTC (noon) and 15:10–15:47 (afternoon). Flight tracks are shown as black contours. The red dot indicates the location of the fjord head reference point for the distance axis used in this study. The second-lowest model level (level 64, mean height 34 m a.s.l.) wind barbs and potential temperature (colour scale) is from CARRA on 19 March at (b) 15:00 and (c) 18:00. The boundary of the land–sea mask from CARRA is shown as a thick purple line in (b) and (c). The topography (grey contours) in (a) is from Amante & Eakins (2009), and in (b) and (c) from CARRA.

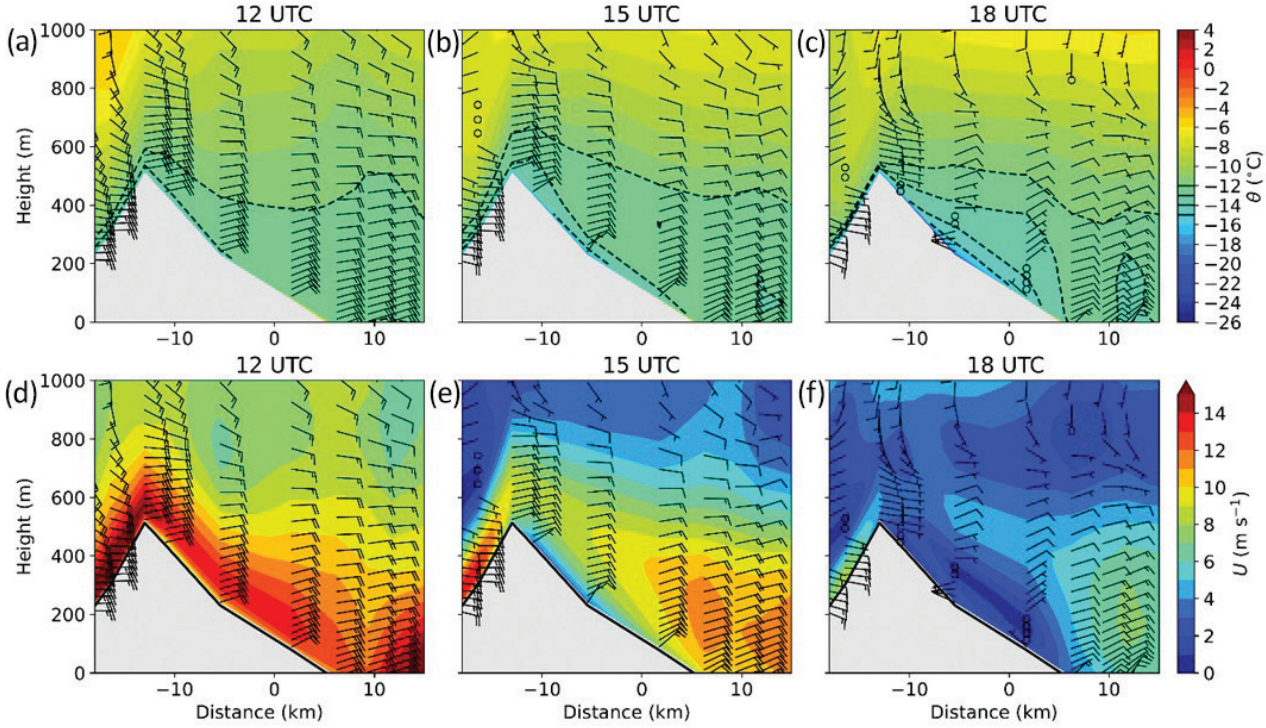

Fig. 13 CARRA (a, f) potential temperature, (d–f) wind speed and wind barbs near the fjord head and south of it—over the mountains—at (a, d) 12:00 UTC, (b, e) 15:00 and (c, f) 18:00. Dashed lines in (a–c) show the isolines of −15, −14, −13 and −12 °C. Wind barbs show the wind direction, as in Fig. 4.

Frank et al. 2025). In two of the cases presented here (19 and 25 March) channelling of the easterly flow to northerly along the fjord axis was observed. In the third case, on 17 March, some channelling also occurred, but easterly winds above the fjord turned to southerly throughout the boundary layer within a horizontal range of ± 20 km around the sea-ice edge in the fjord. In CARRA, the geopotential height gradient over a 100 km distance along the fjord was clearly the highest on 19 March (15.0 m/10.1 m on 19 March during 12:00/18:00, respectively) compared with 6.9 m on 17 March and 8.4 m on 25 March, both at 15:00. Further, on 19 March at 12:00, the easterly wind at 850 hPa level had some northerly component; in all other cases the wind direction was somewhat southerly, from the east–south-east (Supplementary Fig. S1a–d). This explains the northerly flow within the fjord on 19 March. However, since CARRA did not reproduce the channelling effect within the fjord on 17 or on 25 March, it is not possible to evaluate if the higher gradient on 25 March than on 17 March was meaningful for the flow structure within the fjord. Furthermore, since we do not have real observations of winds nor pressure gradients above the fjord, it is not possible to conclude exactly why southerly winds channelled along the fjord on 17 March and northerly winds on 25 March.

Near the surface, a region with southerly winds over the sea ice was observed during all three days. On 17 and 25 March these winds extended beyond the open water in the north, but on 19 March they were observed only in the south in a small part of the fjord. Two processes may contribute to the formation of these near-surface southerly winds within the fjord: (1) drainage flows and katabatic winds originating from the slopes of the surrounding mountains; and (2) an ice-breeze circulation driven by a horizontal surface temperature gradient between open water and sea ice. On the basis of large eddy simulation, Esau & Repina (2012) showed that the thermal contrast in surface temperatures between the glacier and the open water was the main cause for near-surface cold down-valley winds (ice breeze) over Kongsfjorden, Svalbard. Katabatic wind, accelerated by gravity, only had a minor impact on the velocity of the downslope flow.

In this study, the sharp ice edge in the middle of the fjord created favourable conditions for the development of a strong horizontal temperature gradient along the fjord. The radiative cooling and the drainage of cold air from the slopes around the fjord caused a cold-air mass to build up over the sea ice whereas the temperatures over the open water remained relatively warm. The temperature gradient across the sea-ice edge generated a pressure gradient because of the differing air density across the ice edge. In conditions when the effect of the synoptic-scale flow (channelled along the fjord) is weak, the pressure gradient force is the dominant force and an ice breeze (Langland et al. 1989) will develop. This was the situation on 17 and 25 March. On 19 March, the channelled northerly flow was strong and pushed the cold-air mass over the sea ice to the south. In the beginning of the flights, the maximum observed wind speed in the core of the jet of the channelled flow was 13.2 m s^{-1}. Despite such a strong wind, a cold-air pool occurred near the fjord head below about 400 m a.s.l. This was probably due to the Froude number being below one, which Lareau & Horel (2015) have found to be the threshold for the persistence of cold-air pools in valleys. Further, before noon, when the LLJ maximum was observed, the potential temperature increased by 4 K between the lowest measurement height and the height of the LLJ maximum (Δz ca. 550 m). This corresponded to a large bulk-Richardson number of approximately 0.5, indicating strong stability with decoupling between the surface and the air aloft. Indeed, the LLJ was not strong enough to prevent cold air drainage developing on the lowest parts of the Mittag-Lefflerbreen glacier, as southerly winds were observed near the surface at the fjord head and over the mountain slope south of it up to about 80–100 m a.s.l. already before noon.

Most studies of katabatic winds have addressed conditions without ambient winds or with synoptic-scale winds enhancing the katabatic winds (Turner et al. 2009). However, Fitzjarrald (1984) already recognized that strong opposing winds can delay the onset of downslope flows by several hours. Also, during an evening transition with katabatic flow in a river valley, Savage et al. (2008) found that opposing winds lead to shallower slope flows with a smaller horizontal extent, as was the case in our analysis: the layer where down-slope flow was observed at the fjord head increased when the opposing wind became weaker.

The steepness of a slope affects the structure of the katabatic flow (Farina & Zardi 2023). Over gentle slopes, with slope angles (α) about 4° to 6°, katabatic flows are deeper (approximately 100–150 m) than over steep slopes with $\alpha > 20°$, where the flow is shallow, with jet heights only a few metres above the surface. In our study, the surface slope angle below the flight tracks over the Mittag-Lefflerbreen glacier was up to 6°, with a median of 2.5°. The katabatic layer was therefore deep enough to be observed by an aircraft flying a few tens of metres above the surface. To the north of the fjord head, the slopes on both sides of Wijdefjorden are mostly steeper than over the glacier in the south. Based on topographic data from Amante & Eakins (2009), the median slope angle is about 5° between the coastline and the top of the mountains on

Citation: *Polar Research* 2025, *44*, 9263, http://dx.doi.org/10.33265/polar.v44.9263

both sides, but locally the slope angles even exceed 25°. This means that a mixture might occur of very local flow regimes near the surface and wider ones extending to higher levels.

On 19 March, the cold-air mass originally observed in the southern parts of the fjord propagated northwards during the day when the channelled northerly flow weakened. The propagation of the cold air towards the sea-ice edge in the presence of an opposing northerly wind resembles conditions across a sea or lake coastline on a sunny day in the presence of a large-scale offshore wind. Then, a strong surface temperature gradient forms across the coastline due to the different heat capacities of the water and land surfaces, which drives a sea/lake breeze circulation that is opposed by the large-scale offshore flow (Miller et al. 2003). From the beginning to the end of the flight mission on 19 March, a clear deepening of the layer with southerly winds was observed in the cold near-surface air (Fig. 6). Along with the deepening of the southerly flow, the flow speed strengthened as the sea-breeze front propagated northwards. This is in line with the results of Arritt (1993), who found that the strongest sea breezes exist when the sea breeze just reaches the coastline in the presence of a weak to moderate opposing flow. In certain other aspects, however, our results did not follow expectations based on previous studies. Applying the lake breeze index proposed by Biggs & Graves (1962) to our data from the afternoon of 19 March, the opposing northerly wind should have been less than 4 m s^{-1} to allow the northward propagation of the ice-breeze front. The front propagated even though the opposing wind ranged from 4 to 9 m s^{-1}. Neither was the laboratory model of Simpson & Britter (1980)—for the propagation speed of the front—applicable for our case. Using our data, the propagation speed of the front should have been approximately 1 m s^{-1}, but the observed speed was in fact 7 m s^{-1}. The values of the lake breeze index given by Biggs & Graves (1962) and by Simpson & Britter (1980) are in line with the results of Arritt (1993) and Finkele (1998). The deviations from our results are probably due to the complex orography of the fjord. Taking fjord orography into account, Esau & Repina (2012) showed that the opposing wind does not only limit the propagation of the ice breeze down the fjord but also suppresses the layer depth of the down-fjord flow. This was also observed in our study.

The sea-breeze front may have a structure similar to a synoptic-scale cold front (Miller et al. 2003). Atkins et al. (1995) identified two distinct frontal boundaries within a sea-breeze front. The region between the kinematic and thermodynamic fronts is called the thermodynamic frontal zone and is comprised of a mixture of ambient and sea-breeze air masses. Atkins et al. (1995) hypothesize that the frontal zone is generated by a negative circulation pattern ahead of the kinematic front. On 19 March, the two types of fronts were identified on the basis of low-level flights within the fjord. Before noon, when the opposing flow was stronger than in the afternoon, the kinematic front was about 2.0 km southwards from the thermodynamic front, but in the afternoon the width of the frontal zone was only 1.6 km. These distances, are however, much smaller than the width of the frontal zone in the study by Atkins et al. (1995), where it was about 14 km. Crosman & Horel (2010) summarize that a strong offshore wind affects the onshore arrival, extent and the height of the sea breeze, and also leads to a stronger frontogenesis at the leading edge of the sea-breeze front. Hence, we hypothesize that the reason for a narrower frontal zone compared to the observations of Atkins et al. (1995) was the strong opposing wind. However, this contradicts the observation that the frontal zone became narrower from noon to afternoon, when the opposing wind weakened. For the narrowing of front, other factors such as the origin of the flow, from the sides of the fjord (especially in the afternoon), may also be important.

When modelling the ABL within a fjord or in complex terrain, model resolution is an important aspect (Rotach & Zardi 2007; Kilpeläinen et al. 2011; Kilpeläinen et al. 2012; Valkonen et al. 2020). Køltzow et al. (2022) found that the high-resolution CARRA (2.5 km) outperformed ERA5 (31 km resolution) in modelling the 2 m air temperature and 10 m wind speed especially over Svalbard, coastal regions, complex terrain and sea ice. In our study, CARRA reproduced the overall wind channelling in the fjord, but not the smaller details of the flow field, namely, the cold-air pool over the sea ice, the related southerly flow from the fjord head and from Vestfjorden, and the propagation of the cold-air mass towards north in the afternoon of 19 March. This was because of the missing sea ice in CARRA, which led to a large positive bias both in near-surface temperature and wind speed in the southern parts of the fjord. The fjord sea ice was missing in CARRA despite the extrapolation of coarse-resolution satellite data to coastal regions. Although the initial conditions for SST in CARRA, based on OSTIA data with 0.05° resolution, included data points within the fjord, the SIC in southern and central parts of the fjord was also erroneous in OSTIA. In the current version of CARRA, SST is used to filter out sea ice from locations where SST is too high, but not to increase SIC where SST is low.

Results based on CARRA showed that flow channelling and the formation of a katabatic flow can be represented in the model when the grid resolution is 2.5 km. However, realistic modelling of the structure of

gravity currents, both katabatic flows and ice/sea breezes, over complex small-scale orography cannot be solved by a kilometre-scale numerical weather prediction model, because the processes are inherently small-scale and evolve both temporally and spatially (Crosman & Horel 2010; Finnigan et al. 2020). Chen et al. (2019) showed that large-eddy simulation can provide such details in the case of a sea breeze if the model resolution is on the order of 10 m or less.

Conclusions and future perspectives

Unique research aircraft observations revealed complex flow structures within an Arctic fjord on three wintertime days. There were two dominating flow features in this study, the channelling of the large-scale flow up the fjord and the ice-breeze circulation causing down-fjord flow near the surface. In addition, katabatic flow from the surrounding slopes may contribute to the strength of the ice breeze observed within the fjord. Our results suggest that a strong horizontal gradient in temperature across the ice edge was probably the leading driver for the circulation within the fjord. The channelling of the large-scale flow in the fjord can strongly modify the ice-breeze circulation, either by suppressing it to a shallow layer near the surface or in the extreme case push the cold-air mass far towards the sea ice edge. Better understanding is needed on the processes and eventual thresholds of the large-scale wind direction for which the near-surface wind switches from on-ice (up-fjord) to off-ice (down-fjord).

The aircraft observations from Wijdefjorden provide a valuable data set for testing and further developing models in representation of various physical processes and their interactions. These include linkages between the synoptic-scale flow, topography, surface properties and ambient stability, which together affect wind channelling, drainage flows, formation of cold-air pools, as well as on-ice and off-ice flows across a sharp ice edge in a fjord environment.

The lack of sea ice in Wijdefjorden in CARRA prevented the formation of the cold-air pool in the southern parts of the fjord. This highlights the importance of accurate high-resolution sea-ice observations and their assimilation. Substantial improvements in representation of wind and temperature conditions within fjords can be achieved by improving the representation of SIC in atmospheric reanalyses, including future iterations of CARRA.

In the future, Arctic fjord ice will decline because of climate warming and the related increasing inflow of warm (Atlantic) water masses (Skogseth et al. 2020). Furthermore, regional atmospheric dynamics are expected to respond to climate warming, potentially changing the occurrence of up-fjord and down-fjord flows. All these eventual changes would strongly affect the future fjord climate.

Acknowledgements

The authors thank the three anonymous reviewers for their very careful work.

Disclosure statement

The authors report no conflict of interest.

Funding

This research was funded by the European Commission H2020 project Polar Regions in the Earth System (PolarRES; grant no. 101003590) and by the Deutsche Forschungsgemeinschaft (German Research Foundation), Project-ID 268020496 – TRR 172.

References

Amante C. & Eakins B.W. 2009. *ETOPO1 1 Arc-Minute Global Relief Model: procedures, data sources and analysis. NOAA Technical Memorandum NESDIS NGDC-24.* Boulder: Marine Geology and Geophysics Division, National Geophysical Data Center, National Oceanic and Atmospheric Administration.

Arritt R.W. 1993. Effects of the large-scale flow on characteristic features of the sea breeze. *Journal of Applied Meteorology and Climatology 32*, 116–125, doi: 10.1175/1520-0450(1993)032%3C0116:EOTLSF%3E2.0.CO;2.

Atkins N.T., Wakimoto R.M. & Weckwerth T.M. 1995. Observations of the sea-breeze front during CaPE. Part II: dual-Doppler and aircraft analysis. *Monthly Weather Review 123*, 944–969, doi: 10.1175/1520-0493(1995)123<0944:OOTSBF>2.0.CO;2.

Batrak Y., Kourzeneva E. & Homleid M. 2018. Implementation of a simple thermodynamic sea ice scheme, SICE version 1.0-38h1, within the ALADIN-HIRLAM numerical weather prediction system version 38h1. *Geoscientific Model Development 11*, 3347–3368, doi: 10.5194/gmd-11-3347-2018.

Beine H.J., Argentini S., Maurizi A., Mastrantonio G. & Viola A. 2001. The local wind field at Ny-Ålesund and the Zeppelin mountain at Svalbard. *Meteorology and Atmospheric Physics 78*, 107–113, doi: 10.1007/s007030170009.

Biggs W.G. & Graves M.E. 1962. A lake breeze index. *Journal of Applied Meteorology 1 (1962–1982)*, 474–480, doi: 10.1175/1520-0450(1962)001<0474:ALBI>2.0.CO;2.

Brümmer B. & Thiemann S. 2002. The atmospheric boundary layer in an Arctic wintertime on-ice air flow. *Boundary-Layer Meteorology 104*, 53–72, doi: 10.1023/A:1015547922104.

Citation: *Polar Research* 2025, *44*, 9263, http://dx.doi.org/10.33265/polar.v44.9263

Chen G., Iwai H., Ishii S., Saito K., Seko H., Sha W. & Iwasaki T. 2019. Structures of the sea-breeze front in dual-Doppler lidar observation and coupled mesoscale-to-LES modeling. *Journal of Geophysical Research—Atmospheres 124*, 2397–2413, doi: 10.1029/2018JD029017.

Crosman E.T. & Horel J.D. 2010. Sea and lake breezes: a review of numerical studies. *Boundary-Layer Meteorology 137*, 1–29, doi: 10.1007/s10546-010-9517-9.

Donlon C.J., Martin M., Stark J., Roberts-Jones J., Fiedler E. & Wimmer W. 2012. The Operational Sea Surface Temperature and Sea Ice Analysis (OSTIA) system. *Remote Sensing of Environment 116*, 140–158, doi: 10.1016/j.rse.2010.10.017.

Esau I. & Repina I. 2012. Wind climate in Kongsfjorden, Svalbard, and attribution of leading wind driving mechanisms through turbulence-resolving simulations. *Advances in Meteorology 2012*, article no. 568454, doi: 10.1155/2012/568454.

Farina S. & Zardi D. 2023. Understanding thermally driven slope winds: recent advances and open questions. *Boundary-Layer Meteorology 189*, 5–52, doi: 10.1007/s10546-023-00821-1.

Finkele K. 1998. Inland and offshore propagation speeds of a sea breeze from simulations and measurements. *Boundary-Layer Meteorology 87*, 307–329, doi: 10.1023/A:1001083913327.

Finnigan J., Ayotte K., Harman I., Katul G., Oldroyd H., Patton E., Poggi D., Ross A. & Taylor P. 2020. Boundary-layer flow over complex topography. *Boundary-Layer Meteorology 177*, 247–313, doi: 10.1007/s10546-020-00564-3.

Fitzjarrald D.R. 1984. Katabatic wind in opposing flow. *Journal of Atmospheric Sciences 41*, 1143–1158, doi: 10.1175/1520-0469(1984)041<1143:KWIOF>2.0.CO;2.

Flamant C., Drobinski P., Nance L., Banta R., Darby L., Dusek J., Hardesty M., Pelon J. & Richard E. 2002. Gap flow in an Alpine valley during a shallow south föhn event: observations, numerical simulations and hydraulic analogue. *Quarterly Journal of the Royal Meteorological Society 128*, 1173–1210, doi: 10.1256/003590002320373256.

Frank L., Jonassen M.O., Skogseth R. & Vihma T. 2025 Air–sea–ice interactions in Isfjorden, Svalbard: an atmospheric perspective. *Quarterly Journal of the Royal Meteorological Society*, e4956, doi: 10.1002/qj.4956.

Heinemann G. 2018. An aircraft-based study of strong gap flows in Nares Strait, Greenland. *Monthly Weather Review 146*, 3589–3604, doi: 10.1175/MWR-D-18-0178.1.

Heinemann G. & Klein T. 2002. Modelling and observations of the katabatic flow dynamics over Greenland. *Tellus A 54*, 542–554, doi: 10.3402/tellusa.v54i5.12167.

Jonassen M.O., Chechin D., Karpechko A., Lüpkes C., Spengler T., Tepstra A., Vihma T. & Zhang X. 2020. Dynamical processes in the Arctic atmosphere. In A. Kokhanovsky & C. Tomasi (eds.): *Physics and chemistry of the Arctic atmosphere*. Pp.1–51. Cham: Springer.

Kilpeläinen T., Vihma T., Ólafsson H. & Karlsson P.E. 2011. Modelling of spatial variability and topographic effects over Arctic fjords in Svalbard. *Tellus A63*, 223–237, doi: 10.1111/j.1600-0870.2010.00481.x.

Kilpeläinen T., Vihma T., Manninen M., Sjöblom A., Jakobson E., Palo T. & Maturilli M. 2012. Modelling the vertical structure of the atmospheric boundary layer over Arctic fjords in Svalbard. *Quarterly Journal of the Royal Meteorological Society 138*, 1867–1883, doi: 10.1002/qj.1914.

Køltzow M., Schyberg H., Støylen E. & Yang X. 2022. Value of the Copernicus Arctic Regional Reanalysis (CARRA) in representing near-surface temperature and wind speed in the north-east European Arctic. *Polar Research 41*, article no. 8002, doi: 10.33265/polar.v41.8002.

Kristjánsson J.E., Barstad I., Aspelien T., Føre I., Godøy Ø., Hov Ø., Irvine E., Iversen T., Kolstad E., Nordeng T.E., McInnes H., Randriamampianina R., Reuder J., Saetra Ø., Shapiro M., Spengler T. & Ólafsson H. 2011. The Norwegian IPY–THORPEX: polar lows and Arctic fronts during the 2008 Andøya campaign. *Bulletin of the American Meteorological Society 92*, 1443–1466, doi: 10.1175/2011BAMS2901.1.

Langland R.H., Tag P.M. & Fett R.W. 1989. An ice breeze mechanism for boundary-layer jets. *Boundary-Layer Meteorology 48*, 177–195, doi: 10.1007/BF00121789.

Lareau N.P. & Horel J.D. 2015. Turbulent erosion of persistent cold-air pools: numerical simulations. *Journal of the Atmospheric Sciences 72*, 1409–1427, doi: 10.1175/JAS-D-14-0173.1.

Lüpkes C. & Gryanik V.M. 2015. A stability-dependent parametrization of transfer coefficients for momentum and heat over polar sea ice to be used in climate models. *Journal of Geophysical Research—Atmospheres 120*, 552–581, doi: 10.1002/2014JD022418.

Mäkiranta E., Vihma T., Sjöblom A. & Tastula E.-M. 2011. Observations and modelling of the atmospheric boundary layer over sea-ice in a Svalbard fjord. *Boundary-Layer Meteorology 140*, 105–123, doi: 10.1007/s10546-011-9609-1.

Mayr G.J., Armi L., Gohm A., Zängl G., Durran D.R., Flamant C., Gaberšek S., Mobbs S., Ross A. & Weissmann M. 2007. Gap flows: results from the Mesoscale Alpine Programme. *Quarterly Journal of the Royal Meteorological Society 133*, 881–896, doi: 10.1002/qj.66.

Michaelis J., Hartmann J., Schmitt A.U., Birnbaum G., Vihma T. & Lüpkes C. 2023. *High resolution aircraft measurements on three days over Wijdefjorden, Svalbard during the STABLE campaign in March 2013.* Data set. Alfred Wegener Institute, Helmholtz Centre for Polar and Marine Research, Bremerhaven, PANGAEA. Accessed on the internet at https://doi.org/10.1594/PANGAEA.961263 on 30 August 2023.

Michaelis J., Lüpkes C., Schmitt A.U. & Hartmann J. 2021. Modelling and parametrization of the convective flow over leads in sea ice and comparison with airborne observations. *Quarterly Journal of the Royal Meteorological Society 147*, 914–943, doi: 10.1002/qj.3953.

Michaelis J., Lüpkes C., Zhou X., Gryschka M. & Gryanik V.M. 2020. Influence of lead width on the turbulent flow over sea ice leads: modeling and parametrization. *Journal of Geophysical Research—Atmospheres 125*, e2019JD031996, doi: 10.1029/2019JD031996.

Miller S.T.K., Keim B.D., Talbot R.W. & Mao H. 2003. Sea breeze: structure, forecasting, and impacts. *Reviews of Geophysics 41(3)*, article no. 1011, doi: 10.1029/2003RG000124.

Nawri N. & Stewart R.E. 2008. Channelling of high-latitude boundary-layer flow. *Nonlinear Processes in Geophysics 15*, 33–52, doi: 10.5194/npg-15-33-2008.

Queney P. 1948. The problem of air flow over mountains: a summary of theoretical studies. *Bulletin of the American Meteorological Society 29*, 16–26, doi: 10.1175/1520-0477-29.1.16.

Renfrew I.A., Moore G.W.K., Kristjánsson J.E., Ólafsson H., Gray S.L., Petersen G.N., Bovis K., Brown P.R.A., Føre I., Haine T., Hay C., Irvine E.A., Lawrence A., Ohigashi T., Outten S., Pickart R.S., Shapiro M., Sproson D., Swinbank R., Woolley A. & Zhang S. 2008. The Greenland flow distortion experiment. *Bulletin of the American Meteorological Society 89*, 1307–1324, doi: 10.1175/2008BAMS2508.1.

Renfrew I.A., Outten S.D. & Moore G.W.K. 2009. An easterly tip jet off Cape Farewell, Greenland. I: aircraft observations. *Quarterly Journal of the Royal Meteorological Society 135*, 1919–1933, doi: 10.1002/qj.513.

Rotach M.W. & Zardi D. 2007. On the boundary-layer structure over highly complex terrain: key findings from MAP. *Quarterly Journal of the Royal Meteorological Society 133*, 937–948, doi: 10.1002/qj.71.

Savage L.C. III, Zhong S.Y., Yao W.Q., Brown W.J.O., Horst T.W. & Whiteman C.D. 2008. An observational and numerical study of a regional-scale downslope flow in northern Arizona. *Journal of Geophysical Research—Atmospheres 113*, article no. D14114, doi: 10.1029/2007JD009623.

Schnitzhofer R., Norman M., Wisthaler A., Vergeiner J., Harnisch F., Gohm A., Obleitner F., Fix A., Neininger B. & Hansel A. 2009. A multimethodological approach to study the spatial distribution of air pollution in an Alpine valley during wintertime. *Atmospheric Chemistry and Physics 9*, 3385–3396, doi: 10.5194/acp-9-3385-2009.

Schyberg H., Yang X., Køltzow M.A.Ø., Amstrup B., Bakketun Å., Bazile E., Bojarova J., Box J.E., Dahlgren P., Hagelin S., Homleid M., Horányi A., Høyer J., Johansson Å., Killie M.A., Körnich H., Le Moigne P., Lindskog M., Manninen T., Nielsen Englyst P., Nielsen K.P., Olsson E., Palmason B., Peralta Aros C., Randriamampianina R., Samuelsson P., Stappers R., Støylen E., Thorsteinsson S., Valkonen T. & Wang Z.Q. 2020. Arctic regional reanalysis on single levels from 1991 to present. Data set. Copernicus Climate Change Service (C3S) Climate Data Store. Accessed on the internet at https://cds.climate.copernicus.eu/datasets/reanalysis-carra-single-levels?tab=overview on 1 September 2022.

Scorer R.S. 1949. Theory of waves in the lee of mountains. *Quarterly Journal of the Royal Meteorological Society 75*, 41–56, doi: 10.1002/qj.49707532308.

Shestakova A.A., Chechin D.G., Lupkes C., Hartmann J. & Maturilli M. 2022. The foehn effect during easterly flow over Svalbard. *Atmospheric Chemistry and Physics 22*, 1529–1548, doi: 10.5194/acp-22-1529-2022.

Shestakova A.A., Toropov P.A. & Matveeva T.A. 2020. Climatology of extreme downslope windstorms in the Russian Arctic. *Weather and Climate Extremes 28*, article no. 100256, doi: 10.1016/j.wace.2020.100256.

Simpson J.E. & Britter R.E. 1980. A laboratory model of an atmospheric mesofront. *Quarterly Journal of the Royal Meteorological Society 106*, 485–500, doi: 10.1002/qj.49710644907.

Skogseth R., Olivier L.L.A., Nilsen F., Falck E., Fraser N., Tverberg V., Ledang A.B., Vader A., Jonassen M.O., Søreide J., Cottier F., Berge J., Ivanov B. V & Falk-Petersen S. 2020. Variability and decadal trends in the Isfjorden (Svalbard) ocean climate and circulation—an indicator for climate change in the European Arctic. *Progress in Oceanography 187*, article no. 102394, doi: 10.1016/j.pocean.2020.102394.

Suomi I., Lüpkes C., Hartmann J., Vihma T., Gryning S.-E. & Fortelius C. 2016. Gust factor based on research aircraft measurements: a new methodology applied to the Arctic marine boundary layer. *Quarterly Journal of the Royal Meteorological Society 142*, 2985–3000, doi: 10.1002/qj.2880.

Tetzlaff A., Lüpkes C., Birnbaum G., Hartmann J., Nygård T. & Vihma T. 2014. Brief communication: trends in sea ice extent north of Svalbard and its impact on cold air outbreaks as observed in spring 2013. *Cryosphere 8*, 1757–1762, doi: 10.5194/tc-8-1757-2014.

Tetzlaff A., Lüpkes C. & Hartmann J. 2015. Aircraft-based observations of atmospheric boundary-layer modification over Arctic leads. *Quarterly Journal of the Royal Meteorological Society 141*, 2839–2856, doi: 10.1002/qj.2568.

Tonboe R.T., Eastwood S., Lavergne T., Sørensen A.M., Rathmann N., Dybkjær G., Pedersen L.T., Høyer J.L. & Kern S. 2016. The EUMETSAT sea ice concentration climate data record. *The Cryosphere 10*, 2275–2290, doi: 10.5194/tc-10-2275-2016.

Toudal Pedersen L., Dybkjær G., Eastwood S., Heygster G., Ivanova N., Kern S., Lavergne T., Saldo R., Sandven S., Sørensen A. & Tonboe R. 2017. ESA sea ice climate change initiative (Sea_Ice_cci): sea ice concentration climate data record from the AMSR-E and AMSR-2 instruments at 50 km grid spacing, version 2.0. Data set. Centre for Environmental Data Analysis. Accessed on the internet at https://catalogue.ceda.ac.uk/uuid/bc3f8a3cf94c4d0180a60b7e2bfd9c5b/ on 15 September 2022.

Turner J., Chenoli S.N., Abu Samah A., Marshall G., Phillips T. & Orr A. 2009. Strong wind events in the Antarctic. *Journal of Geophysical Research—Atmospheres 114*, article no. D18103, doi: 10.1029/2008JD011642

Valkonen T., Stoll P., Batrak Y., Køltzow M., Schneider T.M., Stigter E.E., Aashamar O.B., Støylen E. & Jonassen M.O. 2020. Evaluation of a sub-kilometre NWP system in an Arctic fjord-valley system in winter. *Tellus, Series A 72*, 1–21, doi: 10.1080/16000870.2020.1838181.

Vihma T., Hartmann J. & Lüpkes C. 2003. A case study of an on-ice air flow over the Arctic marginal sea-ice zone. *Boundary-Layer Meteorology 107*, 189–217, doi: 10.1023/A:1021599601948.

Vihma T., Kilpeläinen T., Manninen M., Sjöblom A., Jakobson E., Palo T., Jaagus J. & Maturilli M. 2011. Characteristics of temperature and humidity inversions and low-level jets over Svalbard fjords in spring. *Advances in Meteorology 2011*, article no. 486807, doi: 10.1155/2011/486807.

Vihma T., Pirazzini R., Fer I., Renfrew I.A., Sedlar J., Tjernström M., Lüpkes C., Nygård T., Notz D., Weiss J., Marsan D., Cheng B., Birnbaum G., Gerland S., Chechin D. & Gascard J.C. 2014. Advances in understanding and parameterization of small-scale physical processes in the marine Arctic climate system: a review. *Atmospheric Chemistry and Physics 14*, 9403–9450, doi: 10.5194/acp-14-9403-2014.

Wendisch M., Macke A., Ehrlich A., Lüpkes C., Mech M., Chechin D., Dethloff K., Velasco C.B., Bozem H., Brückner M., Clemen H.-C., Crewell S., Donth T., Dupuy R., Ebell K., Egerer U., Engelmann R., Engler C., Eppers O., Gehrmann M., Gong X., Gottschalk M., Gourbeyre C., Griesche H., Hartmann J., Hartmann M., Heinold B., Herber A., Herrmann H., Heygster G., Hoor P., Jafariserajehlou S., Jäkel E., Järvinen E., Jourdan O., Kästner U., Kecorius S., Knudsen E.M. Köllner F., Kretzschmar J., Lelli L., Leroy D., Maturilli M., Mei L., Mertes S., Mioche G., Neuber r., Nicolaus m., Nomokonova T., Notholt J., Palm M., van Pinxteren M., Quaas J., Richter P., Ruiz-Donoso E., Schäfer M., Schmieder K., Schnaiter M., Schneider J., Schwarzenböck A., Seifert P., Shupe M.D., Siebert H., Spreen G., Stapf J., Stratmann F., Vogl T., Welti A., Wex H., Wiedensohler A., Zanatta M. & Zeppenfeld S. 2019. The Arctic cloud puzzle: using ACLOUD/PASCAL multiplatform observations to unravel the role of clouds and aerosol particles in Arctic amplification. *Bulletin of the American Meteorological Society 100,* 841–871, doi: 10.1175/BAMS-D-18-0072.1.

Whiteman C.D. & Doran J.C. 1993. The relationship between overlying synoptic-scale flows and winds within a valley. *Journal of Applied Meteorology and Climatology 32*, 1669–1682, doi: 10.1175/1520-0450(1993)032%3C1669:TRBOSS%3E2.0.CO;2.

Yang X., Schyberg H., Palmason B., Bojarova J., Box J., Pagh Nielsen K., Amstrup B., Peralta C., Høyer J., Nielsen Englyst P., Homleid M., Køltzow M.A.Ø., Randriamampianina R., Dahlgren P., Støylen E., Valkonen T., Thorsteinsson S., Kornich H., Lindskog M. & Mankoff K. 2020. *C3S Arctic regional reanalysis: full system documentation*. Accessed on the internet at https://confluence.ecmwf.int/display/CKB/Copernicus+Arctic+Regional+Reanalysis+%28CARRA%29%3A+Full+system+documentation on 12 June 2023.